

Stratigraphy and deformation of Pleistocene talus in relation to a normal fault zone (central Apennines, Italy)

Diethard Sanders*, Hugo Ortner, Hannah Pomella

Institute of Geology, Faculty of Geo- and Atmospheric Sciences, University of Innsbruck, 6030 Innsbruck, Austria

ARTICLE INFO

Article history:

Received 22 March 2018

Received in revised form 25 May 2018

Accepted 25 May 2018

Available online 31 May 2018

Editor: Dr. B. Jones

Keywords:

Quaternary

Apennines

Neotectonism

Faulting

Talus

Coseismic deformation

ABSTRACT

In studies of neotectonism, alluvial-fan and talus deposits commonly are used as deformation markers, but rarely are studied themselves and in relation to adjacent faults. Herein we report on the facies, diagenesis and deformation of a talus succession and fault cataclases in the central Apennines of Italy. The study site is located near the western end of the Assergi normal fault zone that accommodates >2000 m of vertical throw, but was dormant since a longer interval of time.

The preserved talus succession is confined to the fault hangingwall. Deposition and deformation of the talus overlapped with the terminal phase of fault activity. The talus accumulated mainly from grain flows, cohesive debris flows and ephemeral fluid flows; it comprises (i) two superposed units of scree breccias, partly cemented before deformation, and intercalated with (ii) an interval of un lithified scree and soils. The exposed succession accumulated between ≥ 33 –30 cal ka BP to less than ~ 22 cal ka BP. Talus breccias record complex diagenetic successions including eluviation/dissolution of primary matrix, growth of interstitial cements interrupted by episodes of dissolution and/or fracturation, and late-stage dissolution porosity development. Downthrow by faulting produced two types of folds, (i) a syncline-anticline pair with inclined fold axes roughly *normal* to the fault plane, and (ii) a recumbent fold with an axis subparallel to depositional strike of the scree slope; the complicated stratigraphic architecture of the deformed succession is truncated along and hidden beneath the topsoil of the present, uniform slope surface. Further deformation structures include conjugate fractures locally coated by speleothem flowstones, deformation bands, sediment fabrics characterized by planar clast contacts, and lithoclasts crushed *in situ* while embedded in the sediment. Cementation overlapped with and post-dated *in situ* crushing of clasts. The core of the normal fault is an ultracataclasite that (i) shows different degrees of diagenetic recrystallization into micro- to pseudospar, and (ii) that is riddled with solution pores fringed or filled with successive 'generations' of calcite cement. These cements are locally sharply capped along discrete levels, and overlain by ultracataclasite with floating chunks of calcite cement crystals ripped off during increments of faulting. Stable isotopes of oxygen and carbon indicate that the ultracataclasites lithified under influence of meteoric waters, but at variable degrees of rock buffering; the calcite cements within the talus breccias and the flowstones along fractures, in turn, precipitated from meteoric-derived waters with low to negligible rock buffering. The structural juxtaposition of ultracataclasites (probably formed in 1–2 km depth) with talus breccias indicates that the preserved fault/talus ensemble records only the terminal phase of total faulting. The interstitial cements in talus, the flowstones on fracture walls, and the cements in ultracataclasites should be datable with the $^{234}\text{U}/^{230}\text{Th}$ errorchron method. This promises to be a new approach to derive age constraints on talus cementation and fracturation, and on palaeoactivity and final dormance of normal faults.

© 2018 Elsevier B.V. All rights reserved.

1. Introduction

In studies of neotectonic activity, pebbly successions deposited from talus slopes or from alluvial fans typically are used as deformation markers only, but rarely are studied themselves and in their relation to adjacent faults. Talus or scree slopes form by physical weathering of

cliffs, i.e., slopes $>45^\circ$ in dip typically of competent rocks (e.g., Young, 1961; Bates and Jackson, 1980; van Steijn, 2011). In mountain ranges, scree slope development is favoured by (i) presence of high and steep mountain flanks and/or fault scarps, and (ii) rocks that produce scree upon physical weathering; the latter is controlled by the type and structural predisposition of the rock (e.g., jointing, bedding, schistosity) and by environmentally-steered processes, such as deglaciation, rock weakening by thermal fatigue, freeze–thaw cycles, growth of segregation ice, rainfall intensity/distribution, dissolution of carbonate minerals, and vegetation cover (see, e.g., Olyphant, 1983; Kotarba and

* Corresponding author.

E-mail addresses: Diethard.G.Sanders@uibk.ac.at (D. Sanders), Hugo.Ortner@uibk.ac.at (H. Ortner), Hannah.Pomella@uibk.ac.at (H. Pomella).

Strömquist, 1984; Bertran et al., 1995; van Steijn et al., 1995; Watanabe et al., 1998; André, 2003; Hales and Roering, 2005; Sass, 2005; Reid and Thomas, 2006; Krautblatter and Moser, 2009; Moore et al., 2009; Sanders et al., 2009; Molaro and McKay, 2010; van Steijn, 2011; Krautblatter et al., 2012; Ventra et al., 2013; Hall and Thorn, 2014; Sanders et al., 2014). Another process that can markedly influence the accumulation and stratigraphic architecture of scree slopes is syndepositional tectonism.

The effects of syndepositional deformation on scree-slope development can be well-studied in the central Apennines range of Italy. The central Apennines are characterized by intense Pliocene to recent fault activity and numerous earthquakes (Fig. 1) (e.g., Giraudi and Frezzotti, 1995; Galadini and Galli, 2000; Ghisetti and Vezzani, 2002; Galli et al., 2005; Boncio et al., 2010; Gori et al., 2017). Although Pliocene to Quaternary coarse-clastic successions involved in faulting are long-known, in previous studies of neotectonism, these successions were

commonly used as deformation markers only (e.g., Cello et al., 1997; D'Agostino et al., 1998; Galadini and Galli, 2000; Roberts and Michetti, 2004; Galli et al., 2005, 2008; Pizzi et al., 2010; Gori et al., 2011, 2017); their sedimentology, diagenesis and deformation as well as their relation to adjacent faults and fault rocks, in contrast, are hardly documented to date. Herein, we describe a late Pleistocene talus succession subject to normal faulting, folding and diverse types of intrastratal deformation, and its relation to the normal fault zone and associated fault rocks. An approach that integrates the features of deformed pebbly successions with those of the adjacent faults allows for conclusions that go beyond what could be achieved by consideration of only one element, talus or fault. The described deformation features and their relation to faulting should be applicable also to other mountain ranges (provided that caution is taken for potential other effects, such as glacial ice cover) and also are relevant to interpretation of neotectonism in areas of comparatively slower deformation.

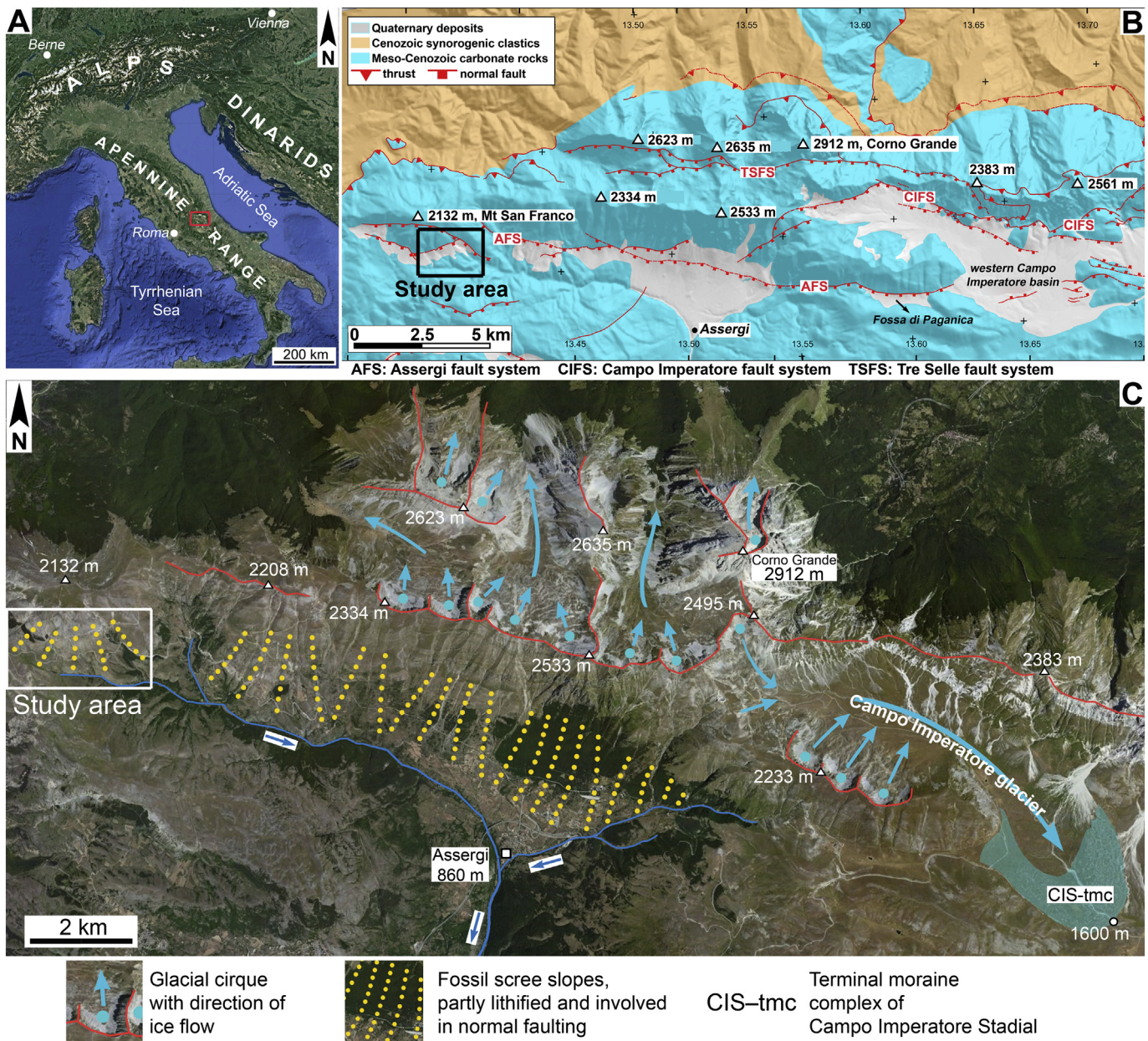


Fig. 1. (A) Position of study area (red rectangle) in Italy. (B) Simplified geological map of Gran Sasso massif, with major fault systems and Quaternary deposits. (C) Selected geomorphic features and Quaternary sediments. Note glacial cirques on north- and east-facing slopes. The long and high south-facing slope north and west of Assergi is covered by fossil scree slopes that are involved in normal faulting.

2. Setting

2.1. Geological substrate

The central Apennines comprise a sector of the NNW-SSE trending mountain range that backbones the Italian peninsula, and consist mainly of Meso-Cainozoic carbonate rocks from shallow-water platform to pelagic basinal settings (Fig. 1A) (e.g., Cardello and Doglioni, 2013). Since the late Miocene these successions were involved, from west to east, in top-NE folding and thrusting (e.g., Lavecchia et al., 1994). Subsequent to erosional truncation of thrust structures along a palaeo-landsurface (e.g., Galadini et al., 2003), uplift and extensional faulting of the central Apennines started during the Pliocene (e.g., Centamore and Nisio, 2003; Gori et al., 2017). A feature of the central Apennines is that thrusting along the leading edge of the orogen is accompanied by uplift and eastward-propagating back-arc NW-SE extension (e.g., Malinverno and Ryan, 1986; Lavecchia et al., 1994; Ferranti et al., 1996; Cavinato and De Celles, 1999; Ghisetti and Vezzani, 1999; Galadini and Messina, 2004; Montone et al., 2004; Galli et al., 2008; Mantovani et al., 2009; Viti et al., 2011; Carminati and Doglioni, 2012). The central Apennines hence became interspersed with fault-bounded half-grabens to symmetrical grabens (Fig. 1B) (e.g., Patacca et al., 1990; Cavinato and De Celles, 1999; Calamita et al., 2000; Galadini and Galli, 2000; D'Addezio et al., 2001; Tondi and Cello, 2003; Papanikolaou et al., 2005; Lavecchia et al., 2017). The major, low-positioned intramontane basins are filled with Pliocene to Quaternary successions, and most of these basins are sediment traps till present (Cavinato et al., 2002; Galadini et al., 2003; Gori et al., 2014), or undergo moderate uplift and erosion (e.g., Gori et al., 2017). The higher-positioned fault basins, in turn, typically are underfilled, and the topographic relief amplitude of fault horsts overall correlates with fault throw (Pizzi, 2003). The flanks of these fault-bounded basins are overlapped by scree slopes and/or alluvial-fan successions (e.g., D'Agostino et al., 1998; Giraudi, 1995; D'Alessandro et al., 2003; Galadini et al., 2003).

In the Gran Sasso area, Meso-Cainozoic carbonate platform to basinal successions became stacked into thrust imbricates with an arcuate

front (e.g., Ghisetti and Vezzani, 1991; Cardello and Doglioni, 2013). Late Messinian folding and thrusting of the area of Gran Sasso was followed by Pliocene to present uplift and extension (Cardello and Doglioni, 2013). In the Gran Sasso, three major normal fault systems are distinguished: (1) the Campo Imperatore system that delimits a half-graben (Campo Imperatore basin; Fig. 1B) individuated during the Early Pleistocene, and persists in activity till present (Giraudi and Frezzotti, 1995; Cavinato and De Celles, 1999; Galli et al., 2002; Roberts and Michetti, 2004; Papanikolaou et al., 2005; Demurtas et al., 2016; Ortner et al., 2018); (2) The Tre Selle system, of less interest in the present context (cf. Giraudi and Frezzotti, 1995), and (3) the Assergi fault system (Fig. 1B) that, in contrast to the first one, is no longer associated with significant basin filling; the Assergi fault appears to be of low historical activity (cf. Cheloni et al., 2010; Blumetti et al., 2013). Aftershocks of the 2009 L'Aquila earthquake showed extensional displacements along the NW end of the Assergi fault zone at depths of approximately 5–10 km, but no surface ruptures were identified along the fault segment described herein (Cheloni et al., 2010; Emergo Working Group, 2010). The cessation of filling of the Assergi basin is related to the fact that (i) the fault hangingwall is drained by perennial streams connected to the L'Aquila–Aterno intramontane basin with a significantly lower local base-level, and (ii) by low activity of faulting. The Assergi fault system probably started during the Early Pleistocene, and remained active at least until the late Pleistocene (see below).

2.2. Quaternary

The Last Glacial Maximum (=Campo Imperatore Stadial, CPS) and subsequent retreat stades is recorded by a complex of recessional moraines at 1600–1620 m a.s.l. (Fig. 1C) (e.g., Adamoli et al., 2010; Giraudi, 2015, his Fig. 6). Radiocarbon ages indicate that, in the central Apennines, the peak last glaciation lasted from 33–27 cal ka BP (Giraudi and Frezzotti, 1997; Giraudi, 2012, 2015). During the CPS, glaciers terminated at 1600 m a.s.l. or higher; this precluded a wholesale glaciation such as in the Alps (e.g., Hughes et al., 2006). In the Gran

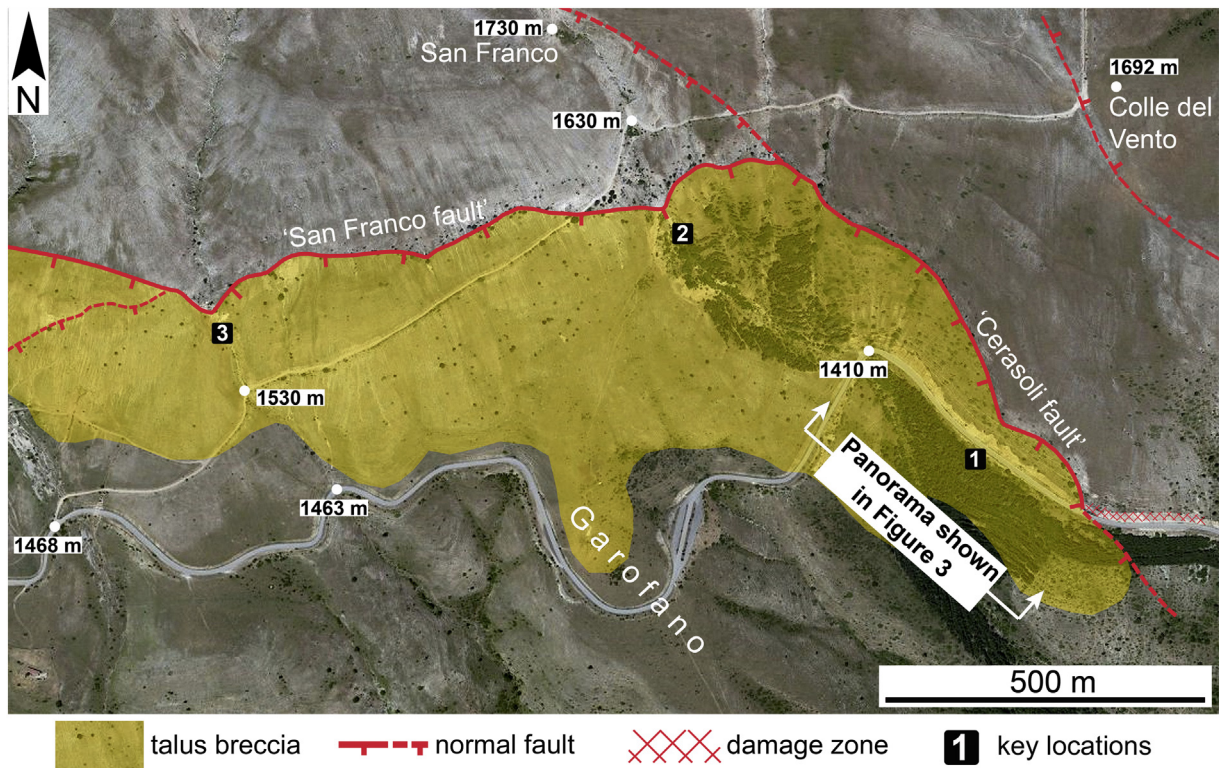


Fig. 2. Distribution of fossil talus breccias near a ridge termed Garofano ('Garofano breccia'). The bedrock succession (without colour) consists of Meso-Cainozoic deep-water limestones that locally contain levels with chert nodules. Numbers 1 to 3 denote key locations described in the text.

Sasso, practically all glacial cirques face towards NE to N (Fig. 1C) (see also Giraudi, 2015). With a single exception, no glacial ice is present today: only in a deep shady cirque directly NE of mount Corno Grande (2912 m, Fig. 1C), the 300-m long (year 2007) Calderone glacier retreats and will be vanished soon (Hughes et al., 2006; Grunewald and Scheithauer, 2010). Conversely, the S-SW facing mountain flanks are devoid of glacial cirques, and show slopes of relatively uniform concave profile with dips from $\sim 40^\circ$ in the upslope part down to a few degrees in the downslope fadeout; these slopes are interspersed with chutes passed by snow avalanches, ephemeral runoff and debris flows (Fig. 1C). Over most of their extent, the S-SW facing slopes are vegetated by grass, as a result of human deforestation (cf., e.g., Borrelli et al., 2013, and references therein). In wintertime, at least the higher areas up from roughly some 1000–1500 m a.s.l. typically are covered by snow. Large

ground-hugging snow avalanches are common, and are evident by features such as crescentic rip-ups of soil and scree in the avalanche starting zones, rock-incised avalanche chutes with polished and striated rock surfaces, toppled and dislodged forest, and isolated boulders laid astray in the distal, low-dipping slope sector of talus cones and alluvial fans. In their middle and lower part, the slopes are mantled by fossil talus successions that were not overridden by glacial ice, but underwent deformation along the Assergi fault zone (Fig. 1B and C). The present climatic regime in the Gran Sasso area is characterized by a lower limit of scree production and gelifraction upward from ~ 2400 – 2500 m a.s.l. (Giraudi, 2005, p. 181 f).

The investigated talus succession is up to a few tens of meters in preserved thickness, and is placed into the Valle Majelama synthem that comprises the Würmian to Holocene interval (see Adamoli et al.,

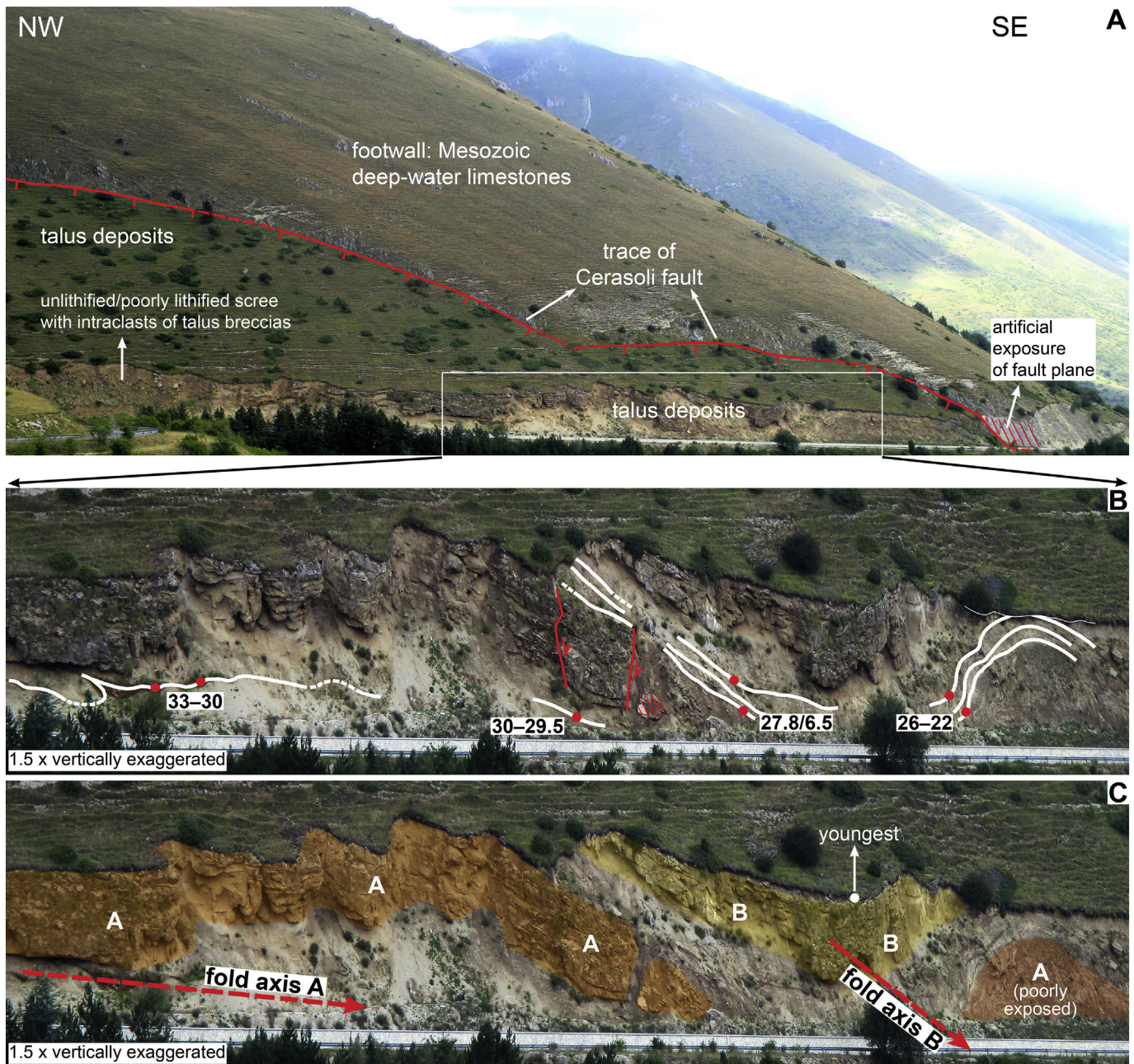


Fig. 3. (A) View onto key outcrop of roadcut along *Strada provinciale Campotosto* (location 1, Fig. 2) showing trace of Cerasoli fault and talus deposits. (B, C) Details to show soil levels (white lines) with maximum–minimum age ranges, and distinct units A and B of talus breccias. The two units are vertically separated by a backweathering interval of poorly-lithified scree with three intercalated soil levels. Note heteroaxial folding of downfaulted succession; approximate fold axes A ($\sim 135/5$ – 10) and B ($\sim 225/30$) not necessarily imply a temporal succession of folding (see text for discussion).

2010). The hangingwall substrate of the studied succession is the Miocene *Marne con Cerroigna* unit (Langhian to Tortonian *pro parte*) of deep-water calcareous marls with calciturbiditic layers. The fault hangingwall consists of Middle Jurassic to Lower Cretaceous deep-water limestones (cf. Adamoli et al., 2010). Among other locations, we had studied the talus and its deformation along the entire Assergi fault system (Fig. 1B). The example selected for more detailed description herein was chosen because of very good 3D-exposure of both talus and faults, combined with presence of soil levels within the talus succession that allow to partly age-bracket scree accumulation and fault-related deformation (Figs. 2 and 3).

3. Methods and definitions

The bedrock, the talus and the faults are shown in the Carta Geologica d'Italia 1:50.000, sheet number 349 Gran Sasso. GPS-pinned data points were indicated in the field in satellite orthophotographs downloaded from Bingmaps®. Orientation data (bedding planes, joints, fault planes and slickensides) were processed with the TectonicVB software (Ortner et al., 2002). Fault planes and linear features (e.g., fold axes) are indicated in dip azimuth/dip notation. Dip azimuth/dip values of fault planes commonly represent the average of two to five measured values. Fourteen samples of talus breccias, nine samples of flowstones along fault surfaces and along fractures within the talus breccias, and ten samples of fault cataclasites were taken to document rock fabrics in cut slabs and thin sections. Thin sections were inspected in plane polarized light, under crossed nicols, and with crossed nicols plus dark-field illumination (photos with light-yellowish tint in figures); in many cases, the latter type of illumination is best suited to display fabrics with fine-grained matrices or the contrast between rock and voids or veins.

Selected samples of ultracataclasites were investigated in backscattered electron microscopy. For inspection, small chips of ultracataclasite were produced by gentle crushing in the laboratory. The chips were cleaned of dust with a jet of pressurized air, then mounted and sputtered with gold. Electron microscopic inspection was done with a Digital Scanning Microscope JEOL JSM-5130LV in low-vacuum mode, at 25 kV acceleration voltage, a gun current of 5 µA, with a backscattered electron detector. For measurement of stable isotopes of oxygen and carbon of diagenetic products and host rocks, 140 samples were excavated from polished slabs with a microdrill. The mass of individual samples weighed for measurement ranged from 5 to 25 mg. Samples were weighed to a precision of ±0.25 µg on a Mettler Toledo UMT2 microbalance, and transferred into round-bottomed borosilicate exetainers. The exetainers then were sealed with butyl rubber septa, and placed into a CTC Combi-Pal autosampler. Measurements were made on a Finnigan DeltaplusXL mass spectrometer connected to a ThermoFinnigan GasBench II. The internal precision (1 sigma) of measurement is typically between 0.03–0.06 for raw δ13C, and 0.04–0.08‰ for raw δ18O; the external precision, calculated over 12 standards per run, typically is 0.05–0.06‰ for δ13C and 0.06–0.08‰ for δ18O. The in-house standard material 'Laas marble' has been calibrated to reference materials NBS-18, NBS-19, CO-1 and CO-8 (see Spötl and Vennemann, 2003, for further details). The soil levels intercalated into the studied talus succession lended themselves for radiocarbon dating. The soils classify as leptosols (WRB classification) or rendzinas (cf. Buol et al., 2011), and are between approximately 10–30 cm in thickness. From the tough and dense soil levels, bulk samples were chiseled out at a depth of 15–20 cm below the surface of the anthropogenic outcrop. Chunks of excavated soil material were put into glass jars or into plastic mugs that were washed with acetone to remove any potential fatty substance. Age dating of bulk samples was done for the sieved (180 µm mesh width) and acid-washed bulk organic fraction. Radiocarbon measurements and age determinations were conducted by Beta Analytic Inc., Miami, United States.

For fault-related rocks, different classifications have been proposed with respect to: (a) a 'cohesive' (lithified) or non-cohesive nature,

(b) content in ultracataclastic matrix, (c) the content and/or size of rock fragments visible with the naked eye, and (d) the presence of foliation or of a non-foliated ('random') fabric (see, Sibson, 1977; Heitzmann, 1985; Woodcock and Mort, 2008). Herein, we use a slightly modified version of the Sibson (1977) classification for designation of brittle-fault fragmented rock. To avoid the use of the term breccia (which otherwise means a solid rock composed of angular fragments) for *incohesive* fractured rock with >30% of visible fragments, we use the term *cacirite* as introduced by Heitzmann (1985). The ultracataclasites along the fault cores described herein show different degrees of diagenetic recrystallization to microspar and pseudospar (Ortner et al., 2018; Sanders et al., 2018). We designate these non-foliated but diagenetically recrystallized rocks as 'sparry ultracataclasites' (Fig. 4). In the following, for sake of brevity, the contact of a fault surface and overlying Quaternary deposits involved in faulting is abbreviated as F/Q contact.

INCOHESIVE	NON-FOLIATED				
	CACIRITE (>30% visible fragments)				
	FAULT GOUGE (<30% visible fragments)				
COHESIVE	PSEUDOTACHYLITE		MATRIX %		
	CATACLASITES	CRUSH BRECCIA (fragments > 5 mm)			
		FINE CRUSH BRECCIA (fragments 1–5 mm)			
		CRUSH MICROBRECCIA (fragments < 1 mm)			
	Grain size reduction by cataclasis			PROTO-CATACLASITE	10-50%
				CATACLASITE	50-90%
ULTRA-CATACLASITE			>90%		
Grain growth by diagenetic recryst.		SPARRY ULTRA-CATACLASITE			

Fig. 4. Modified terminology of disintegrated rock and cataclasites related to brittle faulting. Red are terms introduced herein. See text for description and references.

4. Sedimentary facies

Two groups of talus facies are distinguished (Table 1). (1) Facies group 1 includes (a) breccias with openwork clast fabric, and (b) clast-supported breccias with relicts of an interstitial matrix. The openwork breccias comprise packages up to more than 1 m in thickness of vertically unsharply-delimited strata to gentle lenses identified by differences in mean grain size (Fig. 5A, B and C). In cut slab and thin section, the openwork breccias may be completely devoid of matrix and are entirely lithified by calcite cements (Facies 1A in Table 1) or, aside of cements, contain remnants of an interstitial matrix of lithic wackestone to packstone (Facies 1B in Table 1). Many openwork fabrics show highly heterogeneous clast packing, with patches of densely-packed clasts changing with patches characterized by wide interstitial pore spaces (Fig. 5D). The patches with high clast packing density may show fitted clast boundaries and/or planar contacts between clasts; in addition, the patchy changes of clast packing are accompanied by an absence or scarcity of silt- to sand-sized clasts (Fig. 5D and E). The openwork fabrics typically record complex diagenetic histories characterized by eluviation/dissolution of primary matrix, if present (=Facies 1B), followed by precipitation of successive cement 'generations'; these, in turn, may be separated from each other by episodes of dissolution (Fig. 5F).

(2) Facies group 2, in turn, mainly comprises clast-supported breccias with an interstitial matrix typically of lithic grainstone to packstone to wackestone (Facies 2A in Table 1). In the study area, this facies is comparatively rare, at least in the outweathered lithified parts of the succession (see below for discussion). An uncommon but distinct facies assigned to this category comprises gentle lenses typically a few centimeters in thickness of moderately to very well-sorted, fine to medium-pebbly breccias with a matrix of lithic grainstone to packstone (Fig. 6A and B; Facies 2B in Table 1) These breccias typically are intercalated between bedsets of breccias of other facies types (cf. Fig. 5A and B). In the talus breccias, the degree of lithification and cementation is highly variable, mainly vertically between stratal packages (cf. Fig. 3), but also alongstrike the packages (Fig. 6C).

5. Faults and cataclasites

The roadcut along *Strada provinciale Campotosto* provides the best outcrop of the Cerasoli fault (cf. Figs. 2 and 3). There, an outweathered fault plane on a level of ultracataclasite (fault core) is overlain by an interval a few decimeters in thickness of cacirite; the cacirite, in turn, sharply abuts talus deposits with stratification dragged parallel to the fault surface (Fig. 6D). The fault core locally is coated by flowstone (see below). The natural exposures of the Cerasoli and the San Franco fault (cf. Fig. 2), respectively, are outweathered scarps up to approximately 12 m in height that stand out from the less resistant talus in the fault hangingwall (Fig. 3). Both, the fault footwall and the adjacent damage zones and talus successions in the hangingwall, are cross-cut by incised ravines (Figs. 2, 6E and F).

In Fosso San Franco (location 2, Fig. 2), along the right flank of the ravine, the fault core of the Assergi fault and a triangular damage zone is delimited by the main F/Q surface at the top and a relatively steeper-dipping Riedel splay underneath (Ortner et al., 2014). The cataclasites in this outcrop are layered parallel to the F/Q surface at the top (Fig. 6E). In Fosso Lumitti (location 3, Fig. 2), a similar triangular damage zone as described above is exposed. There, however, lithification is weak and most of the fractured rock is a cacirite (Fig. 6F). Similarly, lithification of the exposed Pleistocene talus above the San Franco fault is poor and patchy. Only in an outcrop of the F/Q surface directly right of Fosso Lumitti, dragged scree is diagenetically welded with a fault cataclasite (Fig. 6F).

The components of fault cataclasites include: (a) carbonate lithoclasts ranging in shape from angular to well-rounded, (b) intraclasts, commonly rounded, of cataclasites, (c) locally, a few angular fragments of chert of pebble- to silt size, and (d) a variable fraction of ultracataclastic matrix. Fault cores are characterized by ultracataclasite and intraclasts derived thereof. The fabrics of (ultra-)cataclasites are more-or-less overprinted by diagenetic recrystallization (microspar to pseudospar crystal fabrics), dissolution resulting in vuggy and vesicular porosity, and precipitation of cement (orthospar). In the roadcut outcrop (location 1, Figs. 2 and 6D), sparry ultracataclasites along the fault core show a 'cloudy' fabric as a result of different degrees of diagenetic

Table 1
Summary of sedimentary facies of talus successions, arranged according to the field appearance of beds. Abbreviations: mgs = mean grain size; sor = sorting (according to Longiaru, 1987).

Clast fabric	Deposit features	Interpretation, references	Remarks
Breccias with openwork clast fabric: Facies group 1	Sheets to lenses few cm's to ~30 cm thick; most clasts with [a,b]-plane parallel to stratification; local downslope or upslope clast imbrication; 'outsize cobbles' may be intercalated. mgs: very fine to coarse pebbles sor: good to moderate, may vary down dip	Facies 1A Deposits of dry and/or aqueous grain flows (= cohesionless debris flows), and of hyperconcentrated flows in channel flow to sheet flow (Lowe, 1976; Gardner et al., 1991; Bertran et al., 1995; Ozouf et al., 1995; van Steijn et al., 1995; Blikra and Nemeč, 1998; Sohn et al., 1999; Benvenuti and Martini, 2002; Sanders et al., 2009; Ouellet and Germain, 2014)	Common facies in the upper, proximal segment of scree slopes This facies comprises an undetermined contribution or overprint by (scree-laden) snow flows and particle creep See Coussot and Meunier (1996) and Dasgupta (2003) for discussion of hyperconcentrated flow category
	Sheets to lenses up to a few dm's thick, may show positive relief; clasts disoriented and may project from bed top; contains patches with interstitial matrix and/or 'non-geopetal', unlaminated matrix of lime mudstone to carbonate-lithic wskt to pkst. mgs: very fine to very coarse pebbles sor: moderate to extremely poor	Facies 1B Originally: Deposits of cohesive debris flows (Fisher, 1971; van Steijn, 1988; van Steijn et al., 1995; Bertran et al., 1997; Blikra and Nemeč, 1998; Sanders et al., 2009)	Common facies from proximal to distal slope segments of scree slopes Secondary openwork fabric: lime-muddy primary matrix was partly eluviated and/or dissolved after deposition Beds of secondary openwork fabric are common
Clast-supported breccias with interstitial matrix: Facies group 2	Sheets to lenses up to a few dm's thick, may show positive relief; clasts disoriented and may project from bed top; matrix is lime mudstone to carbonate-lithic wskt to pkst to grst; matrix typically rich in (cement-fringed) vesicular pores. mgs: very fine to very coarse pebbles sor: moderate to extremely poor	Facies 2A Deposits of cohesive debris flows (references as above)	Common facies from proximal to distal slope segments of scree slope
	Sheets to gentle lenses a few cm's to 10 cm thick. Matrix shows grainstone to packstone texture. mgs: fine to medium pebbles sor: moderate to very good	Facies 2B Deposits of hyperconcentrated flows to low-viscous debris flows (references as above)	Uncommon but distinct; proximal segment of scree slopes

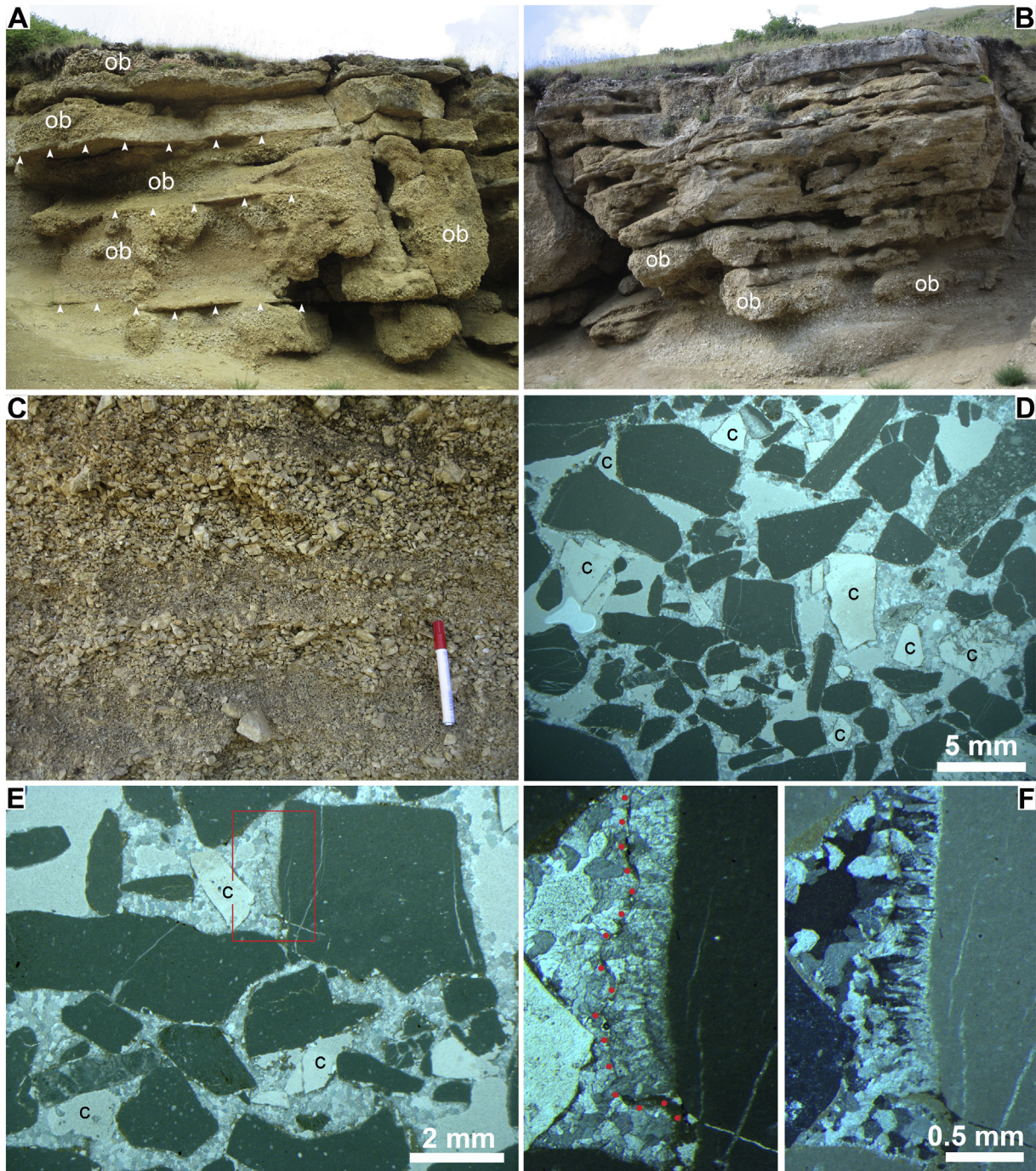


Fig. 5. Talus breccias in field and thin section. (A) Unit A (see Fig. 3B, C): Layers of openwork breccias (ob) are separated by outweathering beds of breccias with a matrix of lithic sand (arrowtips). Width of view 5 m. (B) Unit B (see Fig. 3B, C): Openwork breccias (ob) are overlain by breccias with wavy bedding. Width of view 6 m. (C) Unit B: Set of strata of poorly cemented openwork scree. Stratification is evident mainly by differences in mean grain size. Pen: 14 cm. (D) Thin section of openwork talus breccia. Faintly visible translucent clasts are chert (a few labeled c). Parallel nicols. (E) Detail of preceding photo: Note fitted clast boundaries (c: chert clast). Red rectangle: area of subfigure F. Parallel nicols. (F) Detail of sample shown in subfigure D: Note dissolution surface (red stipples) between successive 'generations' of calcite cement. Left: parallel nicols. Right: Crossed nicols.

recrystallization into micro- and pseudospar (Fig. 7A). Further features of diagenetic overprint include: (a) intrabrecciation related to dissolution, followed by precipitation of calcite cement; (b) fracturation followed by precipitation of calcite cement; and (c) a network of vesicular, open micro- to megapores and vugs up to a few millimeters in width. Repetitive phases of (i) meteoric dissolution, porosity generation and intrabrecciation, changing with (ii) phases of cement precipitation and/or episodic infiltration of lime mud are recorded (Fig. 7A, B, C and D); in addition, (iii) fracturation during diagenetic overprint is recorded by

layers of sharply capped calcite crystals, and/or by fragments of calcite crystals or crystal clusters ripped up from their former cavity and embedded within ultracataclasite (Fig. 7E and F). In SEM, the ultracataclasites show more-or-less isometrical grain size, calcite crystal surfaces, and micropore throats up to a few microns in diameter (Fig. 8A and B).

In Fosso Lumitti (location 3, Fig. 2), as mentioned, nearly the entire exposed damage zone consists of calcirites. Only a patch a few meters in size consists of a crush breccia that is topped by a cataclasite level along the F/Q contact, where a polished slickenside (188/50, 188/48,

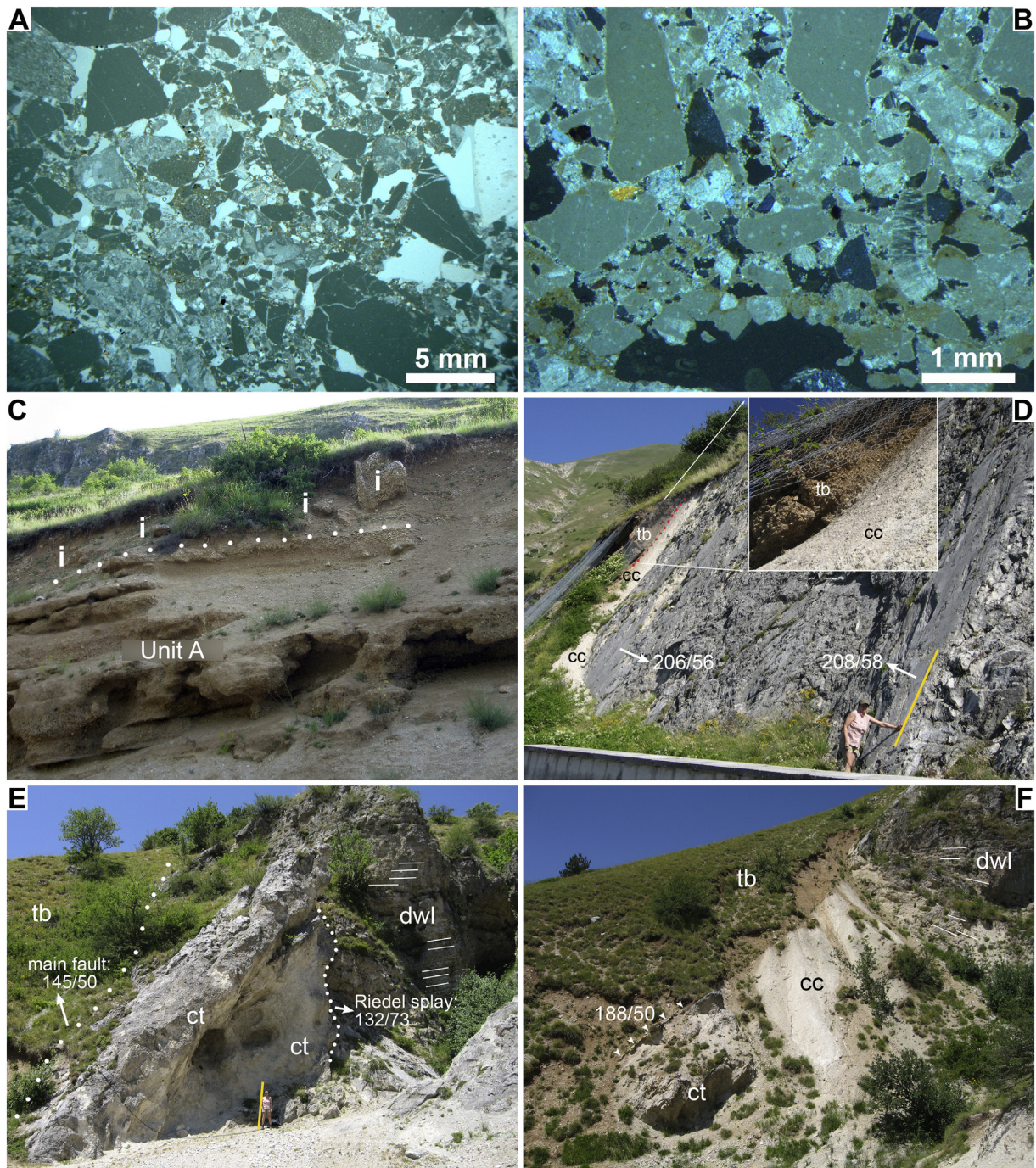


Fig. 6. Talus breccias in field and thin section, and key outcrops of normal faults. (A) Thin section of talus breccia grainstone matrix. Parallel nicols. (B) Detail of preceding photo: Grainstone matrix of mixed calcilithic-chert fragment composition. Crossed nicols. (C) Unit A, NW part. Note variable degree of lithification and backweathering. Dots: boundary between unit A and overlying unlithified scree with large intraclasts (i) of talus breccias. Width of view ~8 m. (D) Roadcut across Cerasoli fault (location 1 in Fig. 2, see Fig. 3): The top of the fault zone is a cacirite (cc) in sharp contact (red stipples) to the downfaulted talus breccia (tb). The fault core is an ultracataclasite. Yellow bar: 2 m. (E) View to NW onto San Franco fault (location 2, Fig. 2): A cataclasite (ct) abuts a succession of deep-water limestones (dwl, white lines show strata) along a Riedel splay (132/73) of the main fault (~145/50) between cataclasite and talus breccia (tb). Yellow bar: 2 m. (F) View to NW onto San Franco fault (location 3, Fig. 2): Cherty deep-water limestones (dwl, white lines show strata) are juxtaposed to a caciritic damage zone (cc) with 'pods' of (proto-)cataclasite (ct). The damage zone is topped by a level of ultracataclasite (white arrowtips) along the fault (188/50), overlain by downfaulted talus breccia (tb). Width of view ~20 m.

186/48) is exposed (cf. Fig. 6F). The crush breccia within this better-lithified patch records a complex diagenetic history characterized by: (a) bedrock fracturation and minor translation-rotation of fragments, (b) illuviation of a brownish matrix of lithic wackestone, (c) meteoric dissolution of clasts and matrix, followed by (d) precipitation of calcite cement and, finally, (e) meteoric dissolution and production of vesicular pores and vugs that cross-cut all older fabrics (Fig. 8C). The cataclasite along the polished slickenside consists of clasts with original rock

fabrics (e.g., fossils), intraclasts of cataclasite to ultracataclasite, and angular chert fragments; adjacent to the slickenside surface, clasts of chert are fragmented down to silt-sized fragments (Fig. 8D).

6. Talus deformation

As described, the degree of talus lithification is highly variable both laterally and vertically. The unlithified intervals of scree (cf. Fig. 3)

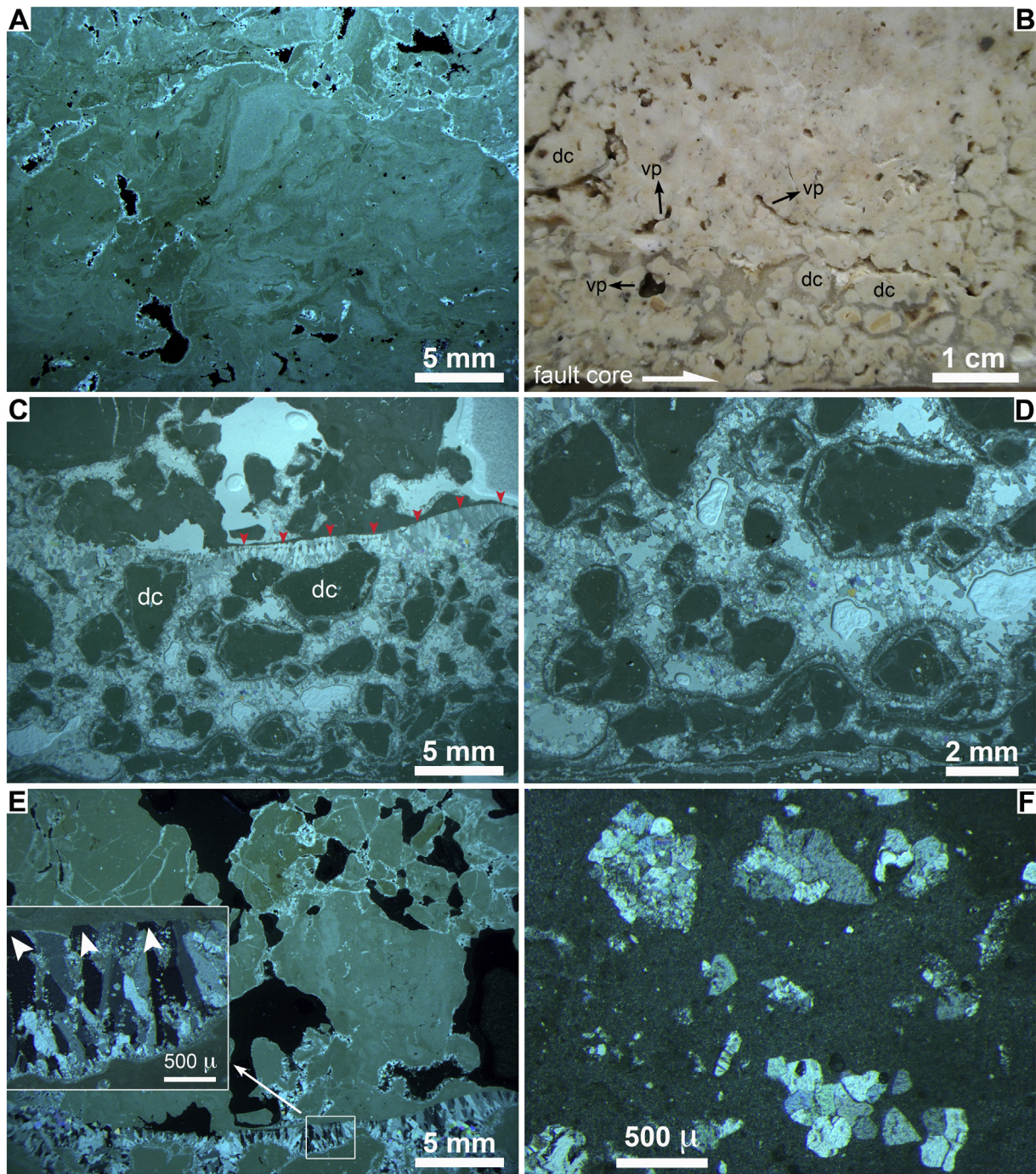


Fig. 7. Microfabrics of fault cores. (A) Thin section of ultracataclasite core of the Cerasoli fault (location 1, Fig. 2). Note (1) cloudy fabric of micrite to microspar to pseudospar, (2) dissolution pores (black) lined by calcite cement, and (3) intrabrecciation by dissolution followed by precipitation of calcite cement. Crossed nicols. (B) Cut slab of ultracataclasite from the Cerasoli fault core. Note intrabreccia of dissolution clasts (a few labeled dc) cemented by calcite, and vesicular open pores (vp, a few labeled by arrows). (C) Thin section of sample of subfigure B. Note (1) dissolution clasts (dc) and interstitial calcite cement, (2) sharp contact (red arrowtips) of truncated calcite crystals to overlying ultracataclasite which, in turn, is riddled by dissolution vugs lined with calcite cement. Parallel nicols. (D) Detail of subfigure C: Solution clasts lined by successive 'generations' of calcite cement that are separated by episodes of dissolution and precipitation of micritic cement. Parallel nicols. (E) Detail of subfigure C: Note sharp boundary between truncated calcite crystals (arrowtips in inset) and overlying ultracataclasite with dissolution vugs (black) and an intrabreccia cemented by calcite. Crossed nicols. (F) Detail of sample shown in subfigure B: Rafts of ripped-up calcite cement float in a matrix of ultracataclasite. Parallel nicols.

reacted on faulting by quasi-homogeneous deformation on a scale of meters and beyond; this deformation, however, was accompanied by *in-situ* fracturation of talus clasts (see below). As obvious from Figs. 2 and 3, the succession was deformed by fault-induced downthrow into folds with strongly different trends of axes. In unit B (cf. Fig. 3), deformation of talus that was unlithified when downfaulted (but lithified after deformation) is recorded by a fault zone a few meters in width that consists

of indistinctly layered scree; within the fault zone, no *in-situ* fracturation of scree clasts was seen (Fig. 8E). Brittle deformation, in turn, of the lithified talus is indicated by fractures that are locally coated by speleothem flowstones (Fig. 8F). In Fosso San Franco (location 2, Fig. 2), the talus deposits show a drag-like decrease of stratal dip: dips of up to $\sim 35^\circ$ near the San Franco fault lessen by concave curvature to dips of 15° – 10° over a plan-view downslope distance of approximately 25–35 m.

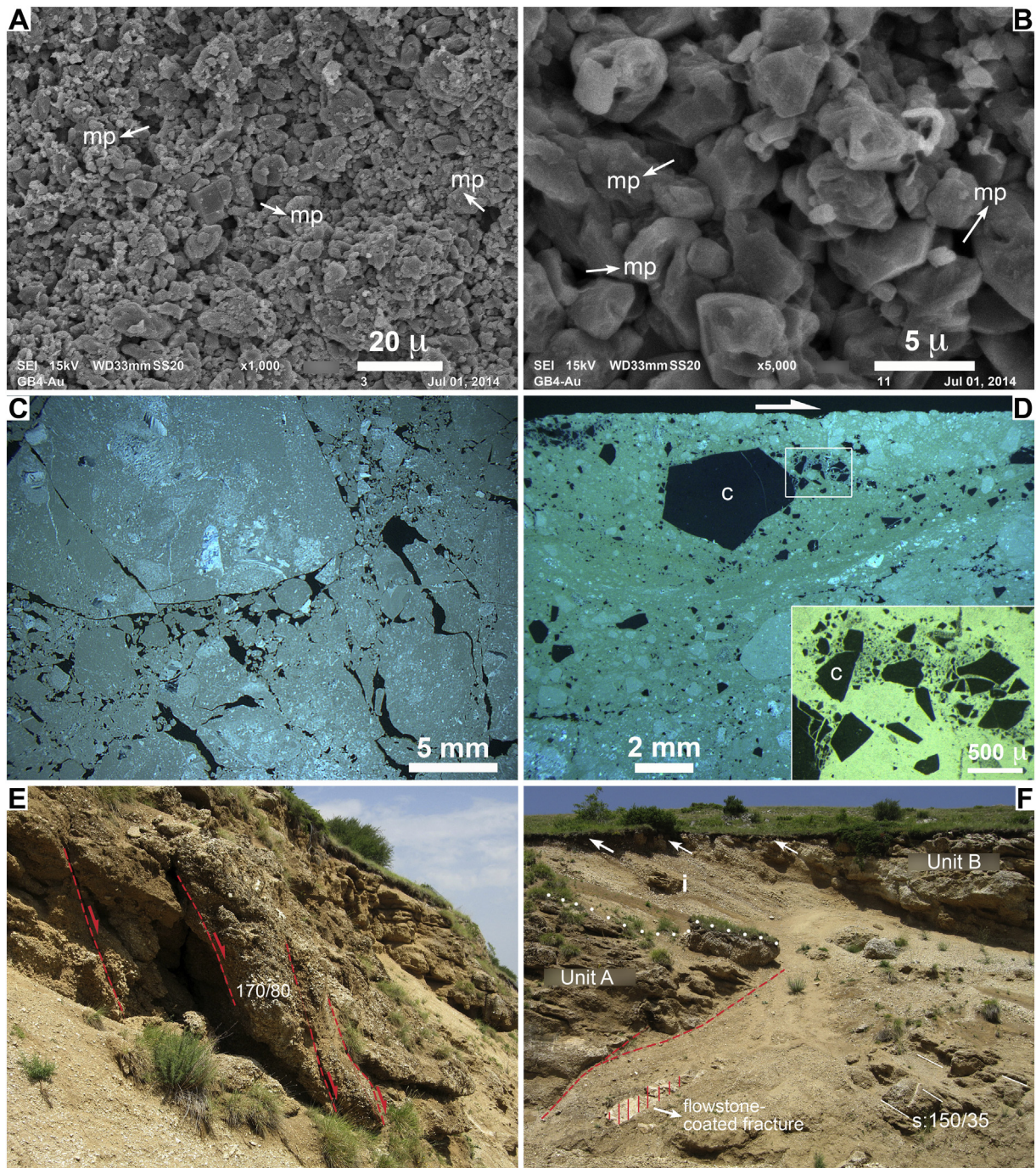


Fig. 8. Microfabrics of fault cores, and faulting of talus. (A, B) Backscattered electron microscopic images of ultracataclasite of Cerasoli fault (location 1, Fig. 2). Note (1) grain sizes from ~10 to 1 μm , (2) micron-scale pores (mp), and (3), that many grains show plane crystal surfaces (subfigure B). (C) Thin section of crush breccia in the fault footwall (location 3, Figs. 2 and 6F): the breccia consists of clasts of deep-water limestones, cemented by thin micrite fringes. Crossed nicols. (D) Thin section of (ultra-)cataclasite along the slickenside (188/50) shown in Fig. 6F. Fragments of deep-water limestones, cataclasites, and of chert (black, one labeled c) within ultracataclastic matrix. Crossed nicols. Inset: Disintegration of chert (c) into silt-sized powder adjacent to the fault plane. Crossed nicols, dark-field illumination. (E) Faults (red dashes) with roughly 170/80, distributed over a deformation zone a few meters in width; no clast fracture was observed. Width of view ~7 m. (F) Roadcut at location 1 (cf. Figs. 2 and 3): Talus breccias of unit A (top: white dots) cut by faults (red dashed lines). Note tilted stratification (s: 150/35) of breccias. Red dashed surface is a fracture coated with speleothem flowstone (see Fig. 11C, D, E and F). Above, an interval of un lithified scree contains levels of soils and intraclasts (i) of talus breccias (cf. Fig. 13D). Note truncation (white arrows) of strata along the soil-covered slope. Width of view ~18 m.

Both in field and thin section, clasts of limestones and chert that were fractured while embedded in the scree are locally common to abundant. *In situ* fracture is indicated by fitted clast boundaries that may be more-or-less dislocated relative to each other. No upper limit of clast size with respect to fracturation was observed; clasts up to at least cobble size were observed that are riddled with fractures. Cracked clasts were most common in strata and stratal packages

of poorly to moderately-sorted, medium- to coarse pebbles with openwork fabric (Fig. 9A–F). In strata of fine pebbles with a sandy matrix, and in strata with a matrix of lithic wackestone to packstone, cracked clasts are more rare. In many cases, relicts of a matrix of lime mudstone to lithic wackestone-packstone are present that indicate that clast fracturation affected also these fabrics (Fig. 10A, B and C). Clast fracturation typically was succeeded by dissolution of

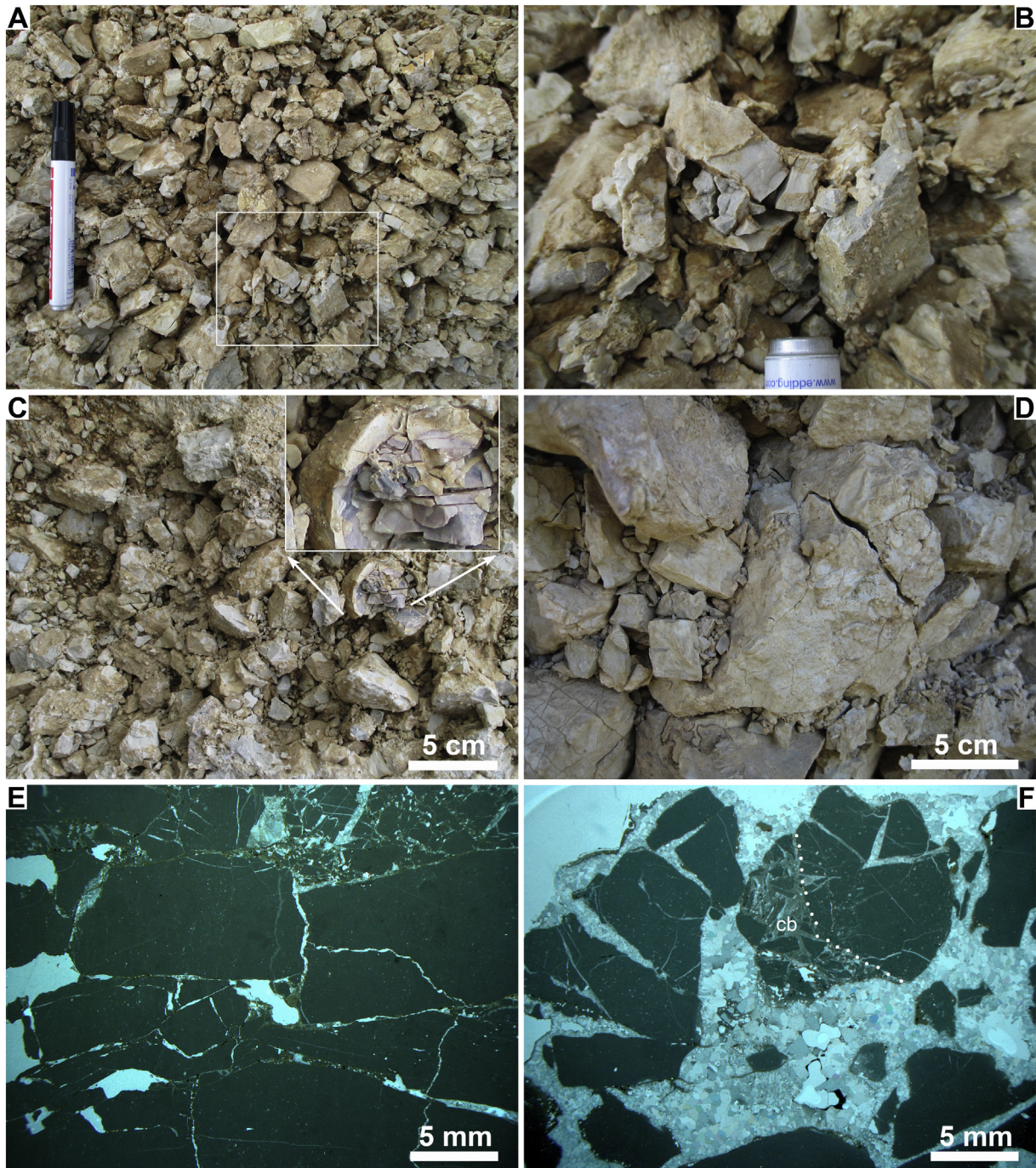


Fig. 9. Talus breccias with crushed lithoclasts. (A) Openwork breccia rich in clasts that were crushed while embedded in the sediment. White rectangle: area of subfigure B. Pen: 14 cm. (B) Detail of crushed clasts. Pen is 1.5 cm in width. (C) Openwork breccia with clasts crushed while embedded in the sediment. Inset: Crushed chert nodule; (D) Openwork breccia with clasts crushed *in situ*. The interstitial space is largely filled with fragments of formerly larger clasts. (E) Thin section of crushed cobble of an openwork breccia at location 2 (cf. Fig. 2). Parallel nicols. (F) Thin section of openwork breccia at location 1 (cf. Fig. 2). Note (1) wide interstitial pore filled with calcite cement, (2) earlier fracture recorded by a cataclastic breccia with matrix (cb, outlined with white stipples), and (3) fitted boundaries and local dissolution pitting of clasts. Parallel nicols.

matrix and clasts, and/or by growth of calcite cements (Fig. 10B, C and D). A further feature indicative of post-depositional overprint of sediment fabric includes patches of densely packed clast fabrics with an estimated clast content up to 55–60% (according to visual estimators in Flügel, 2004); in some cases, dense packing is confined to 'clast pillars' composed of clasts subvertically stacked upon each other along planar contacts (Fig. 10E and F). We observed no clear-cut association of clast cracking with increasing vicinity to faults. Similarly, within a stratum, the vertical and lateral distribution of cracked clasts is not sharply delimited.

7. Flowstones and stable isotope data

The artificially exposed surface of the Cerasoli fault core is locally coated with speleothem flowstone. The flowstone precipitated directly on the ultracataclasite of the fault core. Although vertical changes of speleothem growth fabric are indicated, the flowstone was not subject to later fracture (Fig. 11A and B). Within the talus breccia of unit B, a fracture surface is exposed that is coated by speleothem flowstone up to a few centimeters in thickness (Figs. 3 and 8F). The flowstone is underlain by a talus breccia with clasts fractured *in situ*, and with

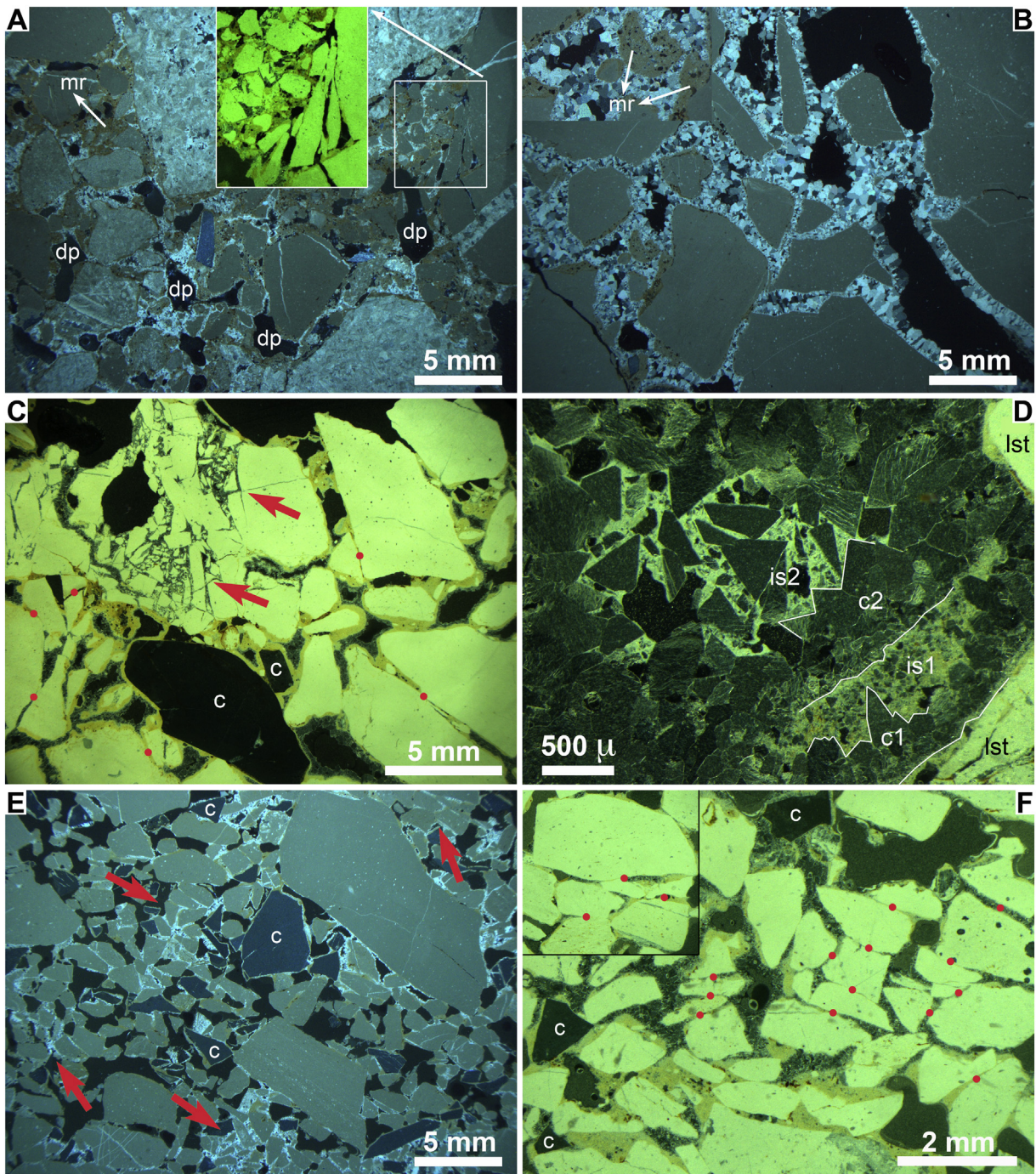


Fig. 10. Crushing of clasts while embedded in the sediment, and multiphase diagenesis. (A) Thin section of talus breccia. Lithoclasts and remnants of an interstitial matrix (mr) overlain by a fringe of calcite cement; clasts, matrix and cement are cut by younger dissolution pores (black, dp). Crossed nicols. Inset: crushing along contact between two clasts. Crossed nicols, dark-field illumination. (B) Thin section of talus breccia with secondary openwork fabric, modified by clast fracturation (location 1, Fig. 2). Note relicts of primary matrix (mr) and dissolution pores (black). Crossed nicols. (C) Thin section of talus breccia. Note (1) crushed clast of limestone (red arrows) above clasts of chert (black, labeled c), and (2) clasts with planar contacts (red dots). Crossed nicols, dark-field illumination. (D) Thin section of talus breccia. Limestone clasts (lst) are overlain by calcite cement (c1), internal sediment (is1, calcite-clastic wacke-to packstone), another cement fringe (c2) and internal sediment (is2) with clasts of calcite crystals. Crossed nicols, dark-field illumination. (E) Thin section of openwork breccia (c: clasts of chert). Note (1) patchy distribution of interstitial cement in densely-packed clast fabrics (arrows), and (2) fitted boundaries of many clasts. Crossed nicols. (F) Patches of clasts with planar contacts (red dots). Scale applies to both images. Crossed nicols, dark-field illumination.

a complex diagenetic history characterized by repetitive phases of dissolution, illuviation of lime mud, cement precipitation and deformation (Fig. 11C and D). The speleothem calcite, in turn, shows an undeformed lower part; upwards, i.e., towards the center of the flowstone-coated fracture, the calcite crystals show progressive deformation twinning and, finally, cataclasis along a level of brittle fracture (Fig. 11E and F).

A total of 140 measurements of stable isotopes of oxygen and carbon of lithoclasts (bedrock) in talus breccias, fault ultracataclasites, cements and speleothem flowstones revealed a clear-cut covariation both of oxygen and carbon towards more negative values (Fig. 12). The isotope values for the lithoclasts as well as for the cements and the flowstones plot within well-defined fields; conversely, the ultracataclasites scatter over a wide range of values. Nevertheless,

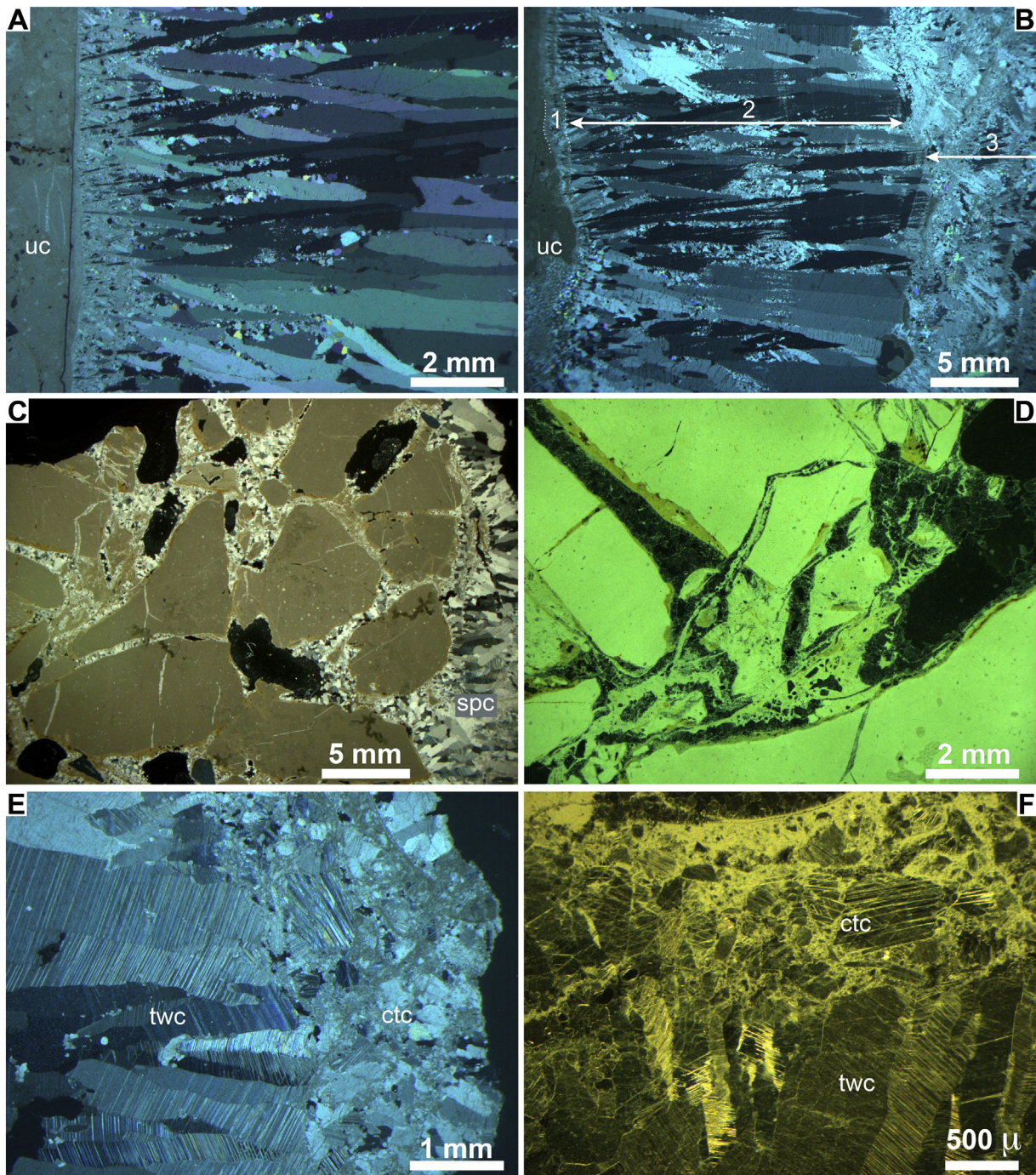


Fig. 11. Fault-coating flowstone and its deformation. (A) Flowstone on the ultracataclasite core (uc) of the Cerasoli fault (cf. Fig. 6D). Crossed nicols. (B) Flowstone on the Cerasoli fault core (cf. Fig. 6D): Ultracataclasite (uc) is overlain by interval 1 of fibrous calcite intercalated with laminae of lime mud, (2) interval 2 of continuous flowstone growth, and (3) interval 3 of dendritic-skeletal calcite and infiltrated lime mud. Crossed nicols. (C) Fractured talus breccia adjacent to flowstone-coated fracture (cf. Fig. 8F). Note fitted clast boundaries fringed by cement. Right margin: Coating of speleothem calcite (spc). Crossed nicols. (D) Detail of subfigure C: Multi-phase fracturation of lithoclasts, cements, and internal sediments. Crossed nicols, dark-field illumination. (E, F) Upper part of flowstone layer (see Fig. 8F). Note twinned calcite crystals (twc) in the lower part, and layer of broken calcite crystals (ctc) along the top. E: Crossed nicols, top to right; F: Crossed nicols, dark-field illumination, top up.

also the values of the ultracataclasites plot along a covariance of oxygen and carbon.

8. Numerical dating

For the soil levels intercalated into the talus succession (Fig. 3), the most consistent ages were derived from the lowest exposed, thick peaty soil that is deformed into a recumbent fold ('lower soil' in Table 2; Fig. 13A). This level varies from 10–50 cm in thickness

and consists of dark brown to blackish, compact, peaty material practically devoid of carbonate rock clasts. For this level, three samples taken along strike yielded a maximum age range between ~33 ka to ~29.5 ka cal BP (see Table 2 for precise figures) (Fig. 13A and B). Because most of the radiocarbon ages center around 30 ka, for sake of brevity, this soil level is briefly designated as '30-ka soil' in the following. Near the SE end of exposure, the '30-ka soil' and its embedding scree is deformed into an array of protrusion-involution structures, and a pipe-like structure composed of scree cross-cuts the soil (Fig. 13C).

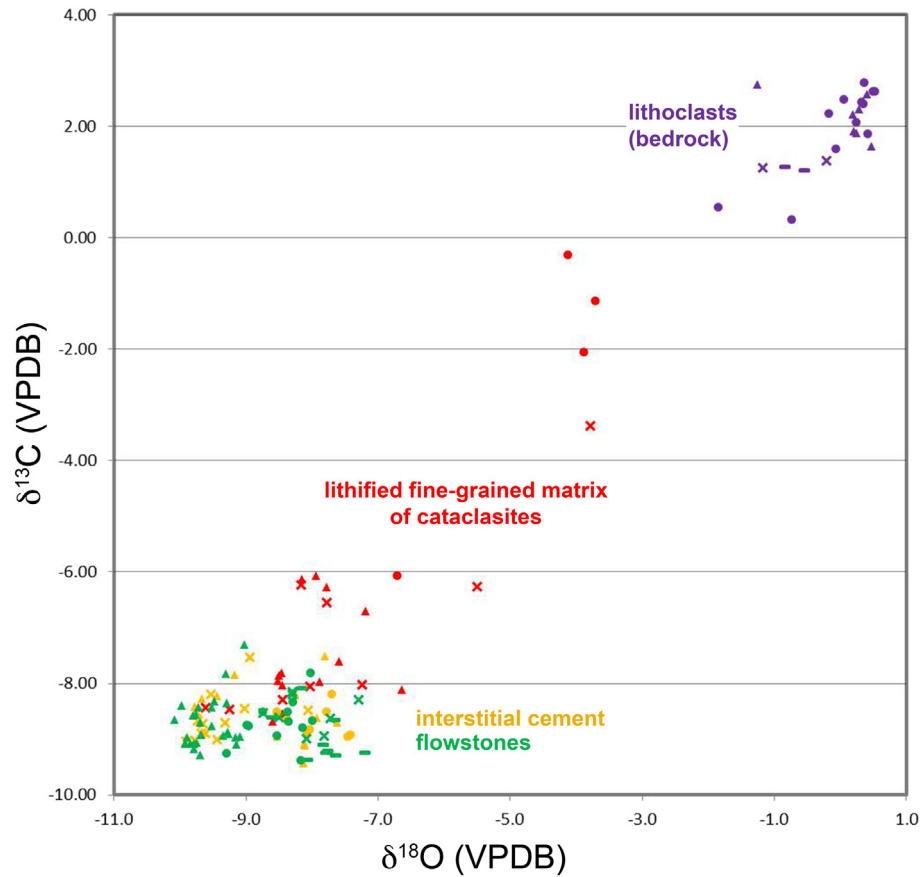


Fig. 12. Plot of stable isotope ratios of oxygen and carbon including: (1) bedrock clasts of talus breccias, (2) fine-grained fault cataclasites, (3) interstitial cements of talus breccias, and (4) flowstone crusts along fractures. Different symbols (dots, crosses, etc.) refer to different rock samples.

Table 2

Radiocarbon ages of sieved and acid-washed organic fraction of soil samples. See Fig. 3B for location of soil intervals.

Position	Field sample code, lab code	Age, cal BP 1950, 95% probability; remarks
'33–29.5 ka soil', NW part of outcrop	GAF 3, Beta-321505	32.780–31.780
'33–29.5 ka soil', NW part of outcrop	GAF 4, Beta-321506	30.540–30.220
'33–29.5 ka soil', NW part of outcrop	GAF 6, Beta-321507	30.140–30.060, 29.790–29.470 Sample was split in lab preparation
'27.8/6.5 k soils', center of outcrop	GRF A, Beta-447524	7.700–7.615 Probably contaminated by younger humic acids infiltrated from pre-roadcut topsoil
'27.8/6.5 k soils', center of outcrop	GRF B, Beta-447525	6.410–6.300 Probably contaminated by younger humic acids infiltrated from pre-roadcut topsoil
'27.8/6.5 k soils', center of outcrop	GRF C, Beta-447526	15.210–15.050 Probably contaminated by younger humic acids infiltrated from pre-roadcut topsoil
'27.8/6.5 k soils', center of outcrop	GRF D, Beta-447527	27.835–27.640
'27.8/6.5 k soils', center of outcrop	G17/1, Beta-471457	20.807–20.440
'27.8/6.5 k soils', center of outcrop	G17/2, Beta-471458	26.980–26.270
'26–22 ka soils', SE end of outcrop	GAS 1, Beta-434146	22.345–21.940
'26–22 ka soils', SE end of outcrop	GAS 2, Beta-43147	23.885–23.435
'26–22 ka soils', SE end of outcrop	GAS 2B, Beta-434148	25.960–25.675

For the comparatively thin 'upper soils' intercalated between unit A and B, respectively (Figs. 3 and 13D), numerical ages scattered strongly (~27.8 to ~6.3 ka cal BP), both between soil levels and among subsamples of the same level (Table 2; Figs. 3 and 13D). In these levels, illuviation of younger humic acids (e.g., from the soil-covered present slope surface removed in roadcut excavation) may have caused a decrease in age. The higher ages determined for the upper soils thus are considered more correct than the younger outlier ages. More consistent ages of ~26 ka to ~22 ka cal BP, in turn, were derived from the 'upper soils' in the SE part of exposure (Fig. 3, Table 2). The package of upper soils thus probably accumulated between approximately 28–22 cal ka BP. A schematic summary of the road outcrop at Cerasoli (location 1, Fig. 2) and the radiocarbon ages is presented in Fig. 14.

9. Interpretation

9.1. Talus facies and diagenesis

As mentioned, the talus succession is characterized by clast-supported fabrics most commonly of openwork type. Openwork fabrics devoid of matrix probably accumulated from grain flows to hyperconcentrated fluid flows (Figs. 5A–F and 6A and B; Facies 1A, Table 1). Similar sediment fabrics with remnants and patches of interstitial matrix, in contrast, are less straightforward to interpret (Fig. 10A and B; Facies 1B, Table 1). The matrix relicts typically are lime mudstone to lithic wackestone. In the Alps similar matrices, albeit in most cases pore-filling, are widespread in talus strata accumulated from cohesive debris flows (Sanders et al., 2009; Sanders, 2010). If the matrix were

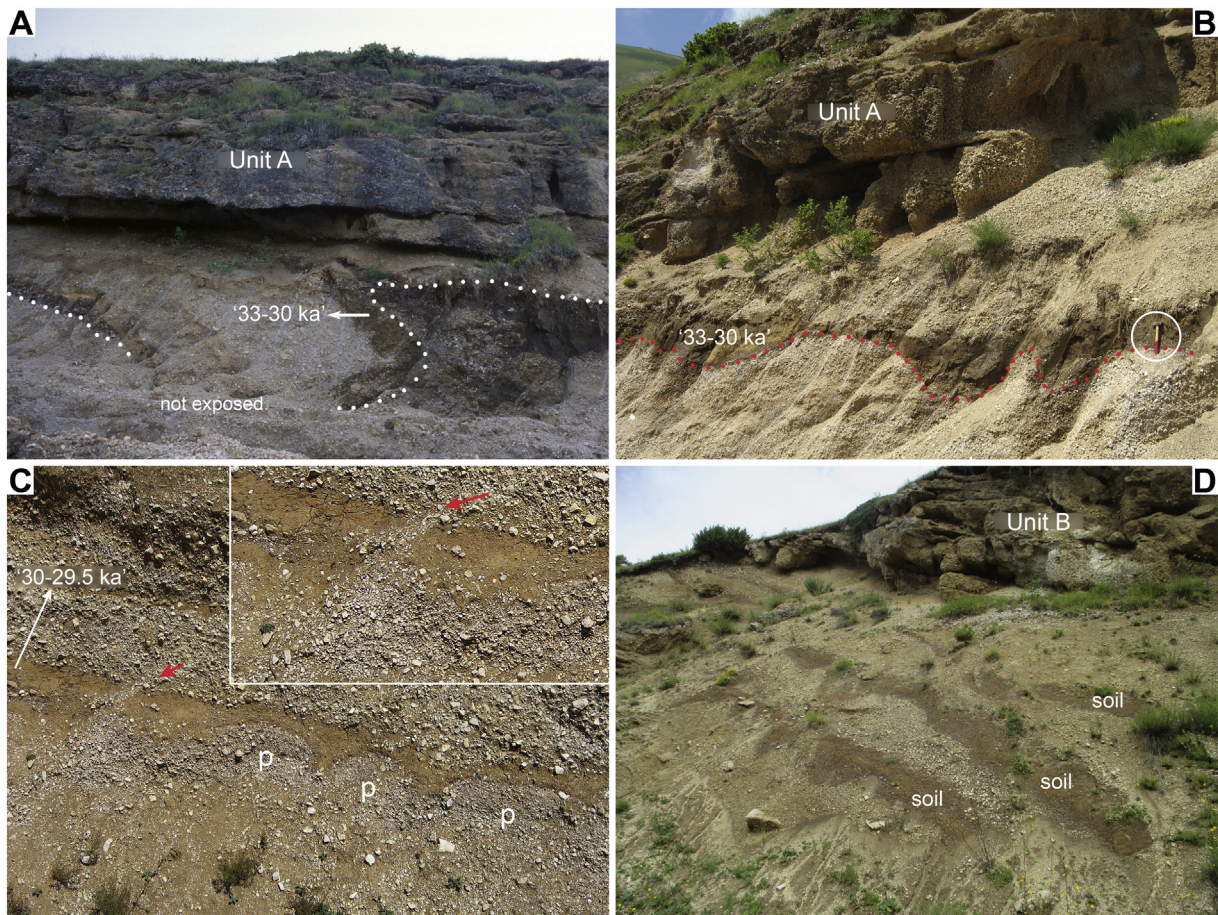


Fig. 13. Soils used to constrain the age of talus deposition. (A) NW part of outcrop 1 (cf. Figs. 3 and 14): Here, the 33–30-ka soil (white dots) is deformed into a recumbent fold that strikes subparallel to the former depositional strike of the scree slope. Width of view ~22 m. (B) Southeastern continuation of the soil shown in subfigure A. Marked pinch and swell probably results from deformation. Hammer (encircled) is 35 cm in length. (C) Outcrop of 30–29.5 ka-soil showing upward-convex protrusions (p) of scree and intercalated involutions of the soil. Red arrow: pipe structure of scree. Width of view 3 m. Inset: Red arrow shows pipe structure of scree that cross-cuts the soil. (D) Three structurally tilted soils ('27.8/6.5-ka soils'; see Figs. 3 and 14) in the package of unlithified scree between unit A and B, respectively (cf. Figs. 3B, C). These soils are truncated at the present slope surface (cf. Figs. 3, 8F and 14). Samples for radiocarbon ages were excavated from the lower and the upper soil level. Above, the outweathered talus breccias of unit B are seen. Width of view in foreground ~10 m.

secondarily illuviated into the interstitial pore space, a geopetal lamination should be seen (e.g., Blikra and Nemec, 1998); even in talus that underwent post-depositional compaction and deformation, secondary matrices show convolute lamination and/or are crushed with lamination still evident (Sanders et al., 2009, 2010b; Sanders, 2016). It is therefore improbable that the lack of geopetal lamination in the pertinent breccia samples from Garofano results from deformation; rather, the relict patches represent vestiges of a primary matrix. Facies 1B thus comprises secondary, partial openwork fabrics produced by eluviation and dissolution of primary matrix. This suggests that facies 1B accumulated from cohesive debris flows that were post-depositionally overprinted. As mentioned, in the study area, large ground-hugging snow avalanches are common, and are recorded by diverse features of erosion and downslope transport of scree and soil. As evident as these features are at surface, however, in most cases it is difficult to clearly identify facies or fabrics related to snow avalanches in fossil talus successions (Sanders et al., 2009, 2014; Sanders, 2013); this holds also for the Garofano breccia. In brief, the Garofano succession accumulated mainly from grain flows, cohesive debris flows, and from fluid flows upon ephemeral surface runoff. Snow-related processes probably were active, too, but could not be positively identified.

The diagenesis of the talus breccias is characterized by matrix eluviation and dissolution and phases of cement precipitation changing with intermittent dissolution and/or fracturation; changes in climate and/or

in tectonic activity and groundwater percolation perhaps underlie these complex diagenetic successions. The covariant stable isotope ratios of oxygen and carbon from talus lithoclasts to interstitial cements and flowstone coatings on fractures indicate that diagenesis was determined by meteoric waters. At least the largest part of calcite carbon thus probably comes from HCO_3^- in meteoric groundwaters, whereas rock-derived carbon contributed only an insignificant fraction. In contrast to the ultracataclasites (see above), this indicates that the diagenetic system in the highly permeable scree-slope successions – mostly openwork fabrics – was open to any change in meteoric diagenetic conditions.

9.2. Faults and cataclasites

As mentioned, the trace of each fault mentioned herein (cf. Fig. 2) is crossed by erosional ravines, and the ravine flanks are graded to the thalwegs. Fault downthrow thus has ceased for an undetermined interval of time. The low footwall scarps, in turn, result from differential erosion of better-lithified limestones and fault cores relative to the downfaulted hangingwall (Figs. 3 and 14) (cf. Fubelli et al., 2009; Bubeck et al., 2015; Kastelic et al., 2017). It is unknown whether the fault footwalls had been covered by scree while faulting was active. Because normal faulting generates hangingwall accommodation space, we suspect that scree covers tend to be thin or absent on footwalls, at least for faults of sizeable throw that provide ample accommodation

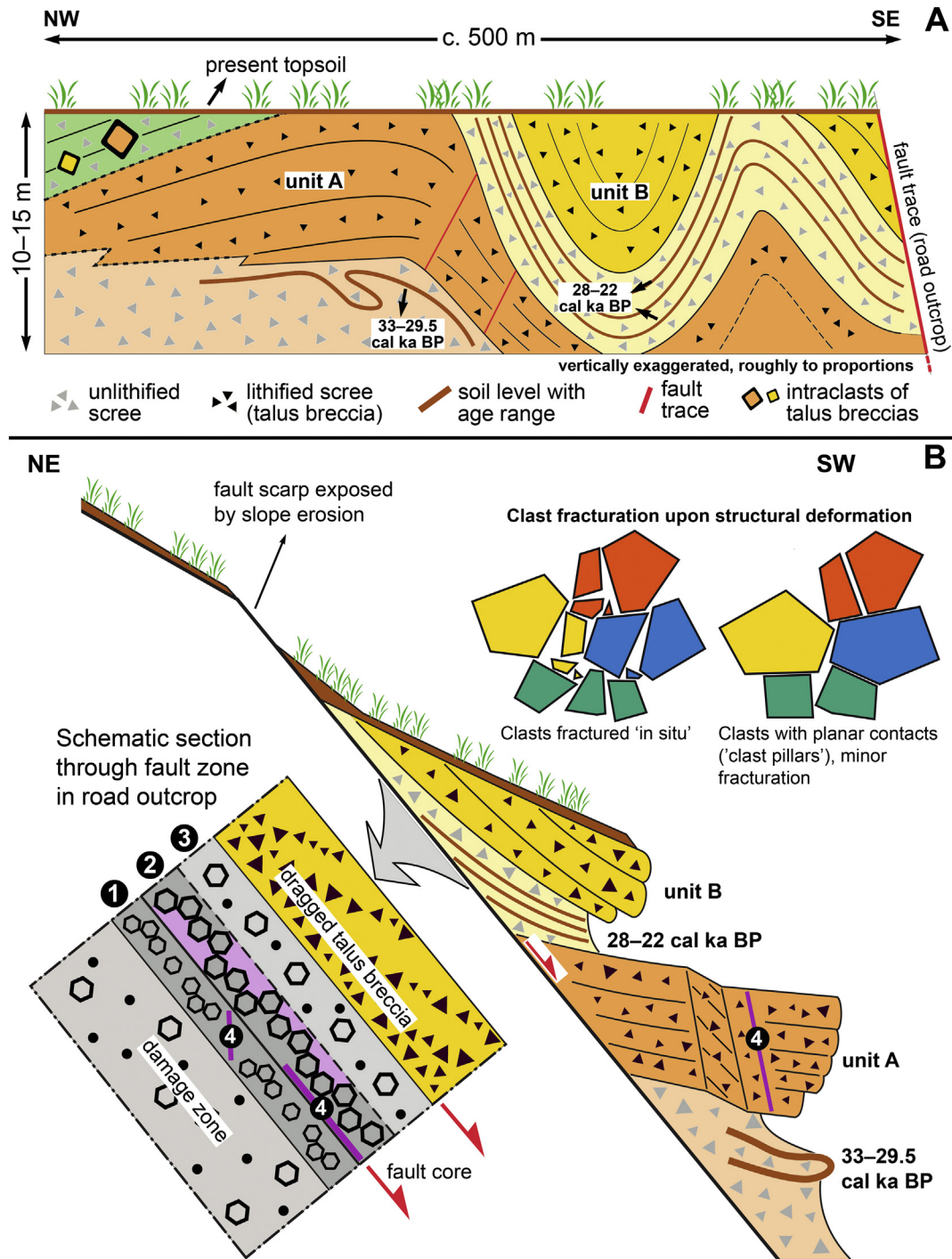


Fig. 14. (A) Summary of stratigraphic architecture and radiocarbon age ranges of soils in the Cerasoli exposure (location 1, Fig. 2, cf. Fig. 3). (B) Sketch of vertical arrangement and deformation, and summary section through Cerasoli fault (cf. Fig. 3). See text for further description and discussion.

space (but see discussion below). Slopes of competent rocks strive to grade to a dip similar to that of the proximal segment of scree slopes (e.g., Summerfield, 1991). Slope erosion subsequent to faulting and talus accumulation thus tends to preserve overall slope dip (Fig. 15), save a potential scarp along the fault core due to differential erosion (Fig. 15) (see Fubelli et al., 2009; Kastelic et al., 2017). A similar slope dip of fault footwalls and talus on hangingwalls is observed not only for the study area, but also along more southern sectors of the dormant Assergi fault and similar fault/talus ensembles in the Central Apennines. The deformation of the talus in the roadcut (location 1, Fig. 2) into folds of roughly rectangular trending relative to each other (fold axis A and B

in Fig. 3, see also Fig. 14) in principle may be explained by a single pulse of downfaulting. Alternatively, the 'syncline-anticline ensemble' and associated soil levels (Fig. 14A) formed *after* the recumbent fold (fold axis A, Fig. 3) of the older '30-ka soil' (Fig. 14B); because of the lateral separation of both fold structures, an unequivocal distinction is hardly possible. In consequence, the radiocarbon ages of soils indicate that deformation of the talus succession took place, either, (a) after ~33 cal ka BP in case of single-phase *folding* (not necessarily single-phase downfaulting), or (b) at least in part subsequent to approximately 22 cal ka BP in case of multi-phase folding. Subsequent to deformation, the succession was truncated along a uniform slope

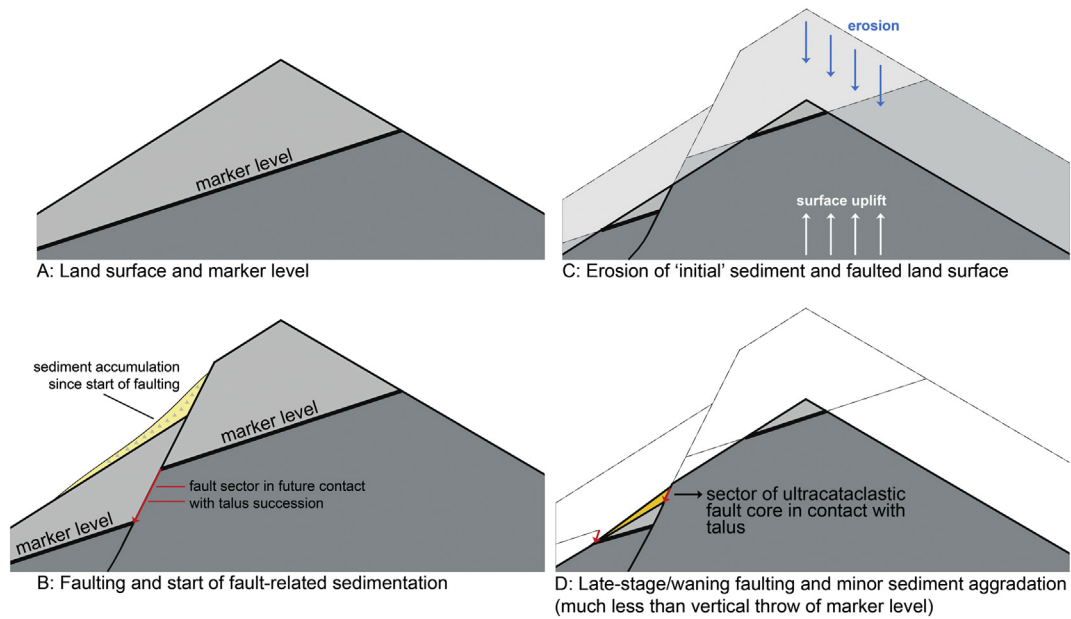


Fig. 15. Hypothesis to explain (1) discrepancy between talus thickness and vertical fault throw, and (2) contact of talus with ultracataclastic fault cores that formed in larger depths. To bring the talus or talus breccias into contact with ultracataclastic fault cores, erosional degradation of the land surface during or after faulting is required. The preserved talus succession in contact with the ultracataclastic fault cores thus accumulated only during the latest increments of fault activity.

covered by the present topsoil (Fig. 14); this underscores that faulting had ceased along the Cerasoli segment for a longer interval of time. To produce the 'syncline-anticline ensemble' with fold axes roughly rectangular to the fault trace, significant along-strike variation of downthrow is required that not necessarily indicates a similar variation of downthrow along the fault in the bedrock underneath (cf. Fig. 15); the lateral variation of downthrow probably result from gravitational deformation (e.g., coseismic sliding/slumping) confined to the talus succession.

Along the fault cores, the calcite-cemented dissolution breccias combined with sharply capped pore-lining cements and rafts of uprooted crystals and crystal clusters of cement embedded within ultracataclastic record increments of fault downthrow (Fig. 7A–F) (Sanders et al., 2018). The ultracataclastic fault cores probably formed in a depth of ~1–2 km (cf. Agosta and Kirschner, 2003, see also Valoroso et al., 2014), i.e., the present F/Q contact in outcrop is not the location of ultracataclastic formation. Rapid displacement under high normal stress is supported by chert pulverized at least down to silt-sized fragments while embedded in carbonate gouge (cf. Fig. 8E). The present F/Q contact thus records terminal or re-activated fault activity plus an unknown amount of erosional slope-surface lowering (Fig. 15). The good lithification of the ultracataclastic fault cores and the co-variation of their oxygen and carbon isotope values (Fig. 12) result from interaction of carbonate-lithic gouge with meteoric waters percolating along the low-permeable ultracataclastic levels (cf. Cello et al., 2001; Ghisetti et al., 2001; Agosta and Kirschner, 2003; Micarelli et al., 2006; Billi, 2010). The wide but co-variant scatter of isotope values most probably results from local differences in rock buffering. Lithification by micron-scale dissolution followed by reprecipitation is supported by the sparry ultracataclasites that comprise patches ranging from microsparite to pseudosparite (Fig. 7A). The electron microscopic investigation of ultracataclasites, showing a crystal fabric with compromise boundaries and micropore throats between crystals (Fig. 8A and B), underscores that they lithified by micron-scale dissolution-reprecipitation. The pore-filling cements in the ultracataclastic intrabreccias and the dissolution vugs, in contrast, show a covariant shift towards negative isotope values of oxygen and carbon that fully overlap with interstitial cements of talus breccias (Fig. 12).

10. Sediment fabrics indicative of deformation

10.1. Talus breccias

The lithoclasts that were cracked while embedded in the sediment – typically in openwork fabrics – are interpreted as a result of coseismic deformation. In contrast to 'strained pebbles' as used in microstructural analysis of coarse-grained deposits, however, the cracked clasts described herein are devoid of striation, solution-pitting and stylolitization (cf., McEwen, 1981; Hippolyte, 2001; Simon, 2007; Bauve et al., 2012). Numerous observations in talus and alluvial-fan successions up to more than 100 m in thickness indicate that mere sediment overburden is not sufficient to induce widespread clast cracking (e.g., Sanders, 2010, 2012; Tuitz et al., 2010); loading by glacial ice streams or coseismic acceleration, in contrast, are documented and modeled to induce clast fracturation (e.g., Eidelman and Reches, 1992; Meyer et al., 2006; Tuitz et al., 2012). In pebbly deposits that were not overridden by a glacier, cracked clasts are most straightforwardly interpreted as a product of tectonic deformation (e.g., Dutour et al., 2002). Coseismic deformation affects clasts via (1) localized simple shear by differential acceleration, combined with (2) generation of strongly fluctuating, high uniaxial stress concentrated at point contacts (Tuitz et al., 2010, 2012; cf. Guises et al., 2009; Sinnott and Cleary, 2009). *In situ* cracking of clasts gives rise to a specific sediment fabric that is readily identified from field to thin section (Figs. 5E, 9, 10, and 14). The described planar contacts between clasts, giving rise to 'clast pillars' composed densely-packed (fracture) clasts, are another feature considered indicative of deformation. This feature is less obvious in the field, but mainly in polished slabs and thin sections. It is interpreted as a result of (cracked) clast re-orientation while embedded within the sediment, and may be accompanied by *in-situ* clast fracture. Re-orientation of clasts may be most easily done by coseismic shaking, but slower deformation might also be efficient in producing these fabrics. The evidence for distinct pulses of clast fracturation and for intermittent fracturation of calcite cements and speleothems records multi-phase deformation of the talus succession. In contrast to the evidence for multi-phase deformation in the fault cores, however, small-scale deformation of the talus breccia not necessarily was tied to active fault slip at site; cracking of clasts and

fracturation of cements may also result from coseismic shaking from strong earthquakes epicentered in the environs.

10.2. 30-ka soil

The upward protrusions of scree and the associated involutions of the 30-ka soil, as well as the pipe-like structure of scree that cross-cuts the soil level (Fig. 13C) are interpreted as structures resulting from liquefaction and fluidization. Liquefaction is defined as a transient change of a resting granular material into a liquefied state (Di Felice, 2010), and is a common phenomenon during earthquakes of magnitude M_s ca. ≥ 4.2 (Galli, 2000). In liquefaction, the different inertia of sediment particles and pore fluid upon coseismic acceleration results in a breakup of the particle fabric, such that grains or grain collectives are supported by fluid for a few moments (Di Felice, 2010; cf. Galli et al., 2008; Hurst et al., 2011). Upon liquefaction of the scree, the scree plus the overlying relatively impermeable soil – impeding pore fluid escape – deformed into an array of scree protrusions and soil involutions (cf. Owen, 1996). Fluidization, in contrast, is defined as *upward* transport of grains or grain collectives suspended within an escaping fluid. The pipe of scree that cross-cuts the soil level thus is interpreted as a fluidization feature (cf. Duranti and Hurst, 2004; Di Felice, 2010; Hurst et al., 2011; Ross et al., 2011). In areas subject to seismic shaking, sediment fabrics indicative of fluidization and/or liquefaction commonly are associated with each other (Owen, 1995, 1996; Mohindra and Bagati, 1996; Obermeier, 1996; Jolly and Lonergan, 2002; Meyer et al., 2006; Hurst et al., 2011).

11. Discussion

If the present contact of the ultracataclastic fault cores (formed under at least 1 km of overburden, see above) with talus corresponded to the original locus of ultracataclasite formation, this would imply that the talus succession should be at least some 1000 m in thickness or more; indeed, however, the preserved succession is up to a few tens of meters in thickness only (see map sheet #349 Gran Sasso). A substantial discrepancy between vertical throw of stratigraphic marker levels in the Meso-Cenozoic succession (~2 km maximum throw along the Assergi fault) and a much smaller thickness of talus successions, combined with the fact that ultracataclastic fault cores are in direct contact with talus breccias, necessitate an overall degradation of land surface, either, while being uplifted, or subsequent to uplift but before the late Pleistocene (cf. Centamore and Nisio, 2003; Galadini et al., 2003) (Fig. 15). As mentioned, significant uplift and normal faulting of the central Apennines started during the Pliocene. If all of the accommodation space generated by downthrow along the Assergi fault had been filled by sediment, a Pliocene to upper Pleistocene succession up to 2 km in thickness should be present, and the lower parts of the preserved succession should be of Pliocene or early Pleistocene instead of late Pleistocene age, respectively. Because the Garofano talus breccias directly overlie the truncated older rock substrate, this indicates that the exposed F/Q contact as well as the talus formed during the last increments of fault activity (Fig. 15). The excellent exposure at Cerasoli indicates that folding and the trends of corresponding fold axes not always follow simple patterns. Because structural downthrow along the fault core at depth was superposed with, or succeeded by, significant

Table 3

Summary of features suggestive of neotectonic or coseismic deformation of pebbly deposits (successions of scree slopes and alluvial fans).

Feature	Characterization	Interpretation	Remarks, figure reference
Drag along contact to fault surface	Strata are dragged upward along contact; stratification may be obliterated by differential movement and re-orientation of clasts	Downthrow of sediment succession along fault surface	May also result from other processes (e.g., compaction or sliding in underlying sediments) not necessarily directly related to coseismic movement Fig. 6D
Folds with strongly different orientation of axes (heteroaxial folds)	Fold axes may trend parallel to normal to displacement direction or to an exposed/presumed fault surface	Heteroaxial folds result from lateral differences in downthrow on a lateral scale of tens of meters to more than 100 m	Lateral differences in downthrow of indicated scale probably result from differential deformation within a sedimentary succession, not differences in downthrow along fault segment; not necessarily related to coseismic movement Fig. 3
Faults/conjugate faults within pebbly succession	Faults and conjugate faults of low offset may be indicated by outweathering 'dykes' up to a few decimeters in thickness that are strongly discordant to stratification; within the dykes, lithoclasts may be intact or cracked Fault planes with striae, Riedel outbreaks and/or fibre calcites are more rare	Faulting in shallow levels of unlithified or poorly lithified successions results in outweathering discordant 'dykes' Faulting in fully lithified talus result in fault surfaces with brittle microtectonic displacement indicators (striae, Riedel outbreaks)	Faulting may proceed also under ice streams, and/or due to differential compaction Fig. 8E and F
Cracked lithoclasts	Clasts cracked <i>in situ</i> while embedded within sediment Typically confined to specific strata or patches therein May occur in distinct 'generations', as indicated by cross-cutting relationships	Clasts are cracked by dynamic overloading during coseismic acceleration	Cracked clasts may also result from loading by overriding ice streams Abundant cracked clasts probably related to earthquakes Figs. 9, 10, 11C and D
'Generations' of interstitial cements	Several 'generations' of interstitial cements that are sharply separated by phases of cement fracturation and dissolution	Growth of interstitial cement became interrupted by coseismic fracture, typically followed by dissolution; then next generation of cement started to precipitate Intraclasts produced by neotectonic disintegration and erosion of lithified talus successions	Cement fracturation may also be induced by other processes (e.g., differential compaction, glacial loading) Figs. 5E and F and 10D
Intraclasts of talus and/or alluvial fan deposits	Clasts up to boulder size of lithified talus or alluvial-fan deposits embedded in younger talus- or fan sediments		Intraclasts are common in the stratigraphically topmost part of talus successions of the central Apennines. Intraclasts may also result from erosional processes unrelated to neotectonism Figs. 6C and 8F
Fractured speleothems	Speleothem flowstones (e.g., along fractures in talus breccias) containing evidence of intermittent fracturation and internal brecciation	Episodic downfaulting or coseismic shaking during speleothem growth	In pebbly successions, fractured speleothems might also result from other processes (e.g., glacial loading, unsteady compaction) Figs. 8F and 11A–F

along-strike variation of downthrow in shallow levels of the talus succession, no simple relation of strike/dip of fold axes of deformed talus with faulting results.

In contrast to many other sedimentary records, scree slopes accumulate on land surface and provide easily-accessible records of neotectonic activity. In mountain ranges that were overridden by glacial ice streams, such as the Alps, however, loading of pre-glacial successions by ice overburden adds much uncertainty to the interpretation of deformation structures (see, e.g., Ampferer, 1936; Ortner, 1996; Costantini and Ortner, 2013). If applied with due caution, however, the study of areas with high rates of structural deformation but limited outreach of glaciers, such as the central Apennines, may support the distinction of features induced by neotectonism from features imparted by glacial loading (Table 3) (Sanders, 2016). All of the diagenetic crystallites observed for the present study – pore-filling cements, flowstones on fracture walls, and ripped-up rafts of cement or flowstone in fault cataclasites – should be datable by the $^{234}\text{U}/^{230}\text{Th}$ disequilibrium method (cf. Geyh, 2005). In the Alps, the U/Th method was successfully applied to age-date interstitial cements of talus breccias and to *ante-quam* date catastrophic rockslides (Ostermann et al., 2007; Sanders et al., 2010a, 2010b; Sanders and Ostermann, 2011; Ostermann and Sanders, 2016; Ostermann et al., 2016). This opens up the new possibility to derive age constraints on talus faulting and fracturation as well as on late phases of fault activity.

12. Conclusions

- (1) In the Gran Sasso area of the central Apennines, we studied a well-exposed fossil talus succession and associated normal faults. Geomorphological evidence indicates that faulting was dormant since a longer interval of time. Radiocarbon ages of intercalated soils show that the upper (exposed) part of the talus succession accumulated during the late Quaternary (≥ 33 –30 cal ka BP to ≤ 22 cal ka BP).
- (2) The normal faults that abut the downfaulted talus show ultracataclastic fault cores. In the ultracataclasites, late phases of incremental downthrow are recorded by (i) intraclasts of ultracataclasite, (ii) pore-filling calcite cements sharply capped along discrete levels and overlain by (iii) ultracataclasite with floating crystals and crystal clusters of formerly pore-lining cements that were uprooted during fault reactivation.
- (3) The talus comprises clast-supported pebbly deposits of grain flows, cohesive debris flows and ephemeral fluid flows; snow-related processes could not be positively identified. Diagenetic successions are complex; they are characterized by eluviation/dissolution of matrix, corrosion of lithoclasts, precipitation of different 'generations' of calcite cements (in many cases separated by intermittent dissolution), and late-stage solution porosity. Diagenesis overlapped in time with talus deformation.
- (4) Except for two ravines, the soil-covered present top surface of the downfaulted talus succession is relatively smooth, and belies a complicated deformation underneath. In a roadcut, the succession displays two types of decameter-scale folds, (i) a recumbent fold with an axis subparallel to depositional strike (and subparallel to fault strike), and (ii) an anticline-syncline pair with axes that rake roughly perpendicular to the fault plane.
- (5) Aside of fault-related downthrow, drag, and folding, the talus deposits are cut by conjugate joints and faults. One fault is coated by speleothem flowstone which, in turn, was involved in fracturation. In addition, lithoclasts that were cracked while embedded in the sediment are abundant, and probably result from coseismic deformation.
- (6) The juxtaposition of ultracataclasites that probably formed in 1–2 km depth with talus breccias indicates that the preserved fault/talus ensemble records only the terminal phase of total downfaulting.
- (7) Stable isotopes of oxygen and carbon of ultracataclasites, pore-lining cements and speleothems indicate that diagenesis of the fault cataclasites and of the talus succession proceeded under influence of meteoric waters. The cements in the ultracataclasites and in the talus breccias should be datable with the $^{234}\text{U}/^{230}\text{Th}$ method. This may help to derive age constraints on talus accumulation and on palaeoactivity and dormance of faults.

Acknowledgements

The constructive comments of an anonymous reviewer and of the editor Brian Jones are gratefully acknowledged.

References

- Adamoli, L., Calamita, F., Pizzi, A., et al., 2010. Note illustrative della Carta geologica d'Italia alla scala 1:50.000, foglio 349 Gran Sasso d'Italia. Servizio Geologico d'Italia, Roma, p. 255.
- Agosta, F., Kirschner, D.L., 2003. Fluid conduits in carbonate-hosted seismogenic normal faults of central Italy. *Journal of Geophysical Research* 108 (B4):2221. <https://doi.org/10.1029/2002JB002013>.
- Ampferer, O., 1936. Beiträge zur Geologie der Hungerbergterrasse bei Innsbruck. *Jahrbuch der Geologischen Bundesanstalt* 86, 353–358.
- André, M.-F., 2003. Do periglacial landscapes evolve under periglacial conditions? *Geomorphology* 52, 149–164.
- Bates, R.L., Jackson, J.A., 1980. *Glossary of Geology*. American Geological Institute, Falls Church (Va) (749 pp.).
- Bauve, V., Rolland, Y., Sanchez, G., Giannerini, G., Schreiber, D., Corsini, M., Perez, J.-L., Romagny, A., 2012. Pliocene to Quaternary deformation in the Var Basin (Nice, SE France) and its interpretation in term of "slow-active" faulting. *Swiss Journal of Geosciences* 105, 361–376.
- Benvenuti, M., Martini, I.P., 2002. Analysis of terrestrial hyperconcentrated flows and their deposits. In: Martini, I.P., Baker, V.R., Garzón, G. (Eds.), *Flood and Megaflood Processes and Deposits: Recent and Ancient Examples*. Special Publications of the International Association of Sedimentologists 32, pp. 167–193.
- Bertran, P., Francou, B., Texier, J.P., 1995. Stratified slope deposits: the stone-banked sheets and lobes model. In: Slaymaker, O. (Ed.), *Steepland Geomorphology*. John Wiley & Sons, Chichester, pp. 147–170.
- Bertran, P., Héty, B., Texier, J.-P., van Steijn, H., 1997. Fabric characteristics of subaerial slope deposits. *Sedimentology* 44, 1–16.
- Billi, A., 2010. Microtectonics of low-P low-T carbonate fault rocks. *Journal of Structural Geology* 32, 1392–1402.
- Blikra, L.H., Nemeč, W., 1998. Postglacial colluvium in western Norway: depositional processes, facies and palaeoclimatic record. *Sedimentology* 45, 909–959.
- Blumetti, A.M., Guerrerri, L., Vittori, E., 2013. The primary role of the Paganica–San Demetrio fault system in the seismic landscape of the middle Aterno Valley basin (Central Apennines). *Quaternary International* 288, 183–194.
- Boncio, P., Pizzi, A., Brozzetti, F., Pomposo, G., Lavecchia, G., Di Naccio, D., Ferrarini, F., 2010. Coseismic ground deformation of the 6 April 2009, L'Aquila earthquake (central Italy, Mw6.3). *Geophysical Research Letters* 37, L06308. <https://doi.org/10.1029/2010GL042807>.
- Borrelli, P., Hoelzmann, P., Knitter, D., Schütt, B., 2013. Late Quaternary soil erosion and landscape development in the Apennine region (central Italy). *Quaternary International* 312, 96–108.
- Bubeck, A., Wilkinson, M., Roberts, G.P., Cowie, P.A., McCaffrey, K.J.W., Phillips, R., Sammonds, P., 2015. The tectonic geomorphology of bedrock scarps on active normal faults in the Italian Apennines mapped using combined ground penetrating radar and terrestrial laser scanning. *Geomorphology* 237, 38–51.
- Buol, S.W., Southard, R.J., Graham, R.C., McDaniel, P.A., 2011. *Soil Genesis and Classification*. Wiley-Blackwell, Chichester (543 pp.).
- Calamita, F., Coltorti, M., Piccinini, D., Pierantoni, P.P., Pizzi, A., Ripepe, M., Scisciani, V., Turco, E., 2000. Quaternary faults and seismicity in the Umbro-Marchean Apennines (Central Italy): evidence from the 1997 Colfiorito earthquake. *Journal of Geodynamics* 29, 245–264.
- Cardello, G.L., Doglioni, C., 2013. From Mesozoic rifting to Apennine orogeny: the Gran Sasso range (Italy). *Gondwana Research* 27, 1307–1334.
- Carminati, E., Doglioni, C., 2012. Alps vs. Apennines: the paradigm of a tectonically asymmetric Earth. *Earth-Science Reviews* 112, 67–96.
- Cavinato, G.P., De Celles, P., 1999. Extensional basins in the tectonically bimodal central Apennines fold-thrust belt, Italy: response to corner flow above a subducting slab in retrograde motion. *Geology* 27, 955–958.
- Cavinato, G.P., Carusi, C., Dall'Asta, M., Miccadei, E., Piacentini, T., 2002. Sedimentary and tectonic evolution of Plio-Pleistocene alluvial and lacustrine deposits of Fucino Basin (central Italy). *Sedimentary Geology* 148, 29–59.
- Cello, G., Mazzoli, S., Tondi, E., Turco, E., 1997. Active tectonics in the central Apennines and possible implications for seismic hazard analysis in peninsular Italy. *Tectonophysics* 272, 43–68.
- Cello, G., Tondi, E., Micarelli, L., Invernizzi, C., 2001. Fault zone fabrics and geofluid properties as indicators of rock deformation modes. *Journal of Geodynamics* 32, 543–565.

- Centamore, E., Nisio, S., 2003. Effects of uplift and tilting in the Central-Northern Apennines (Italy). *Quaternary International* 101–102, 93–101.
- Cheloni, D., D'Agostino, N., D'Anastasio, E., Avallone, A., Mantenuto, S., Giuliani, R., Mattone, M., Calcaterra, S., Gambino, P., Dominici, D., Radicioni, F., Fastellini, G., 2010. Coseismic and initial post-seismic slip of the 2009 Mw 6.3 L'Aquila earthquake, Italy, from GPS measurements. *Geophysical Journal International* 181, 1539–1546.
- Costantini, D., Ortner, H., 2013. Klüfte und Deformationsstrukturen in jungpleistozänen Beckensedimenten des Rißtales, Bayern. *Geo. Alp* 10, 5–26.
- Coussot, P., Meunier, M., 1996. Recognition, classification and mechanical description of debris flows. *Earth-Science Reviews* 40, 209–227.
- D'Addezio, G.D., Masana, E., Pantosti, D., 2001. The Holocene paleoseismicity of the Aremogna-Cinque Miglia Fault (Central Italy). *Journal of Seismology* 5, 181–205.
- D'Agostino, N., Chamot-Rooke, N., Funicello, R., Jolivet, L., Speranza, F., 1998. The role of pre-existing thrust faults and topography on the styles of extension in the Gran Sasso range (central Italy). *Tectonophysics* 292, 229–254.
- D'Alessandro, L., Miccadei, E., Piacentini, T., 2003. Morphostructural elements of central-eastern Abruzzi: contributions to the study of the role of tectonics on the morphogenesis of the Apennine chain. *Quaternary International* 101–102, 115–124.
- Dasgupta, P., 2003. Sediment gravity flow—the conceptual problems. *Earth-Science Reviews* 62, 265–281.
- Demurtas, M., Fondriest, M., Balsamo, F., Clemenzi, L., Storti, F., Bistacchi, A., Di Toro, G., 2016. Structure of a normal seismogenic fault zone in carbonates: the Vado di Corno Fault, Campo Imperatore, Central Apennines (Italy). *Journal of Structural Geology* 90, 185–206.
- Di Felice, R., 2010. Liquid-solid suspension theory with reference to possible applications in geology. *Basin Research* 22, 591–602.
- Duranti, D., Hurst, A., 2004. Fluidization and injection in the deep-water sandstones of the Eocene Alba Formation (UK North Sea). *Sedimentology* 51, 503–529.
- Dutour, A., Philip, H., Jaurand, E., Combes, P., 2002. Mise en évidence de déformations en faille inverse avec ruptures de surface cosismiques dans des dépôts colluviaux würmiens du versant nord du mont Ventoux (Provence occidentale, France). *Comptes Rendus Geoscience* 334, 849–856.
- Eidelman, A., Reches, Z., 1992. Fractured pebbles—A new stress indicator. *Geology* 20, 307–310.
- Emergo Working Group, 2010. Evidence for surface rupture associated with the Mw 6.3 L'Aquila earthquake sequence of April 2009 (central Italy). *Terra Nova* 22, 43–51.
- Ferranti, L., Oldow, J.S., Sacchi, M., 1996. Pre-Quaternary orogen-parallel extension in the Southern Apennine belt, Italy. *Tectonophysics* 260, 325–347.
- Fisher, R.V., 1971. Features of coarse-grained, high-concentration fluids and their deposits. *Journal of Sedimentary Petrology* 41, 916–927.
- Flügel, E., 2004. *Microfacies of Carbonate Rocks*. Springer, Berlin, p. 976.
- Fubelli, G., Gori, S., Falucci, E., Galadini, F., Messina, P., 2009. Geomorphic signatures of recent normal fault activity versus geological evidence of inactivity: case studies from the central Apennines (Italy). *Tectonophysics* 426, 252–268.
- Galadini, F., Galli, P., 2000. Active tectonics in the Central Apennines (Italy)—Input data for seismic hazard assessment. *Natural Hazards* 22, 225–270.
- Galadini, F., Messina, P., 2004. Early-Middle Pleistocene eastward migration of the Abruzzi Apennine (central Italy) extensional domain. *Journal of Geodynamics* 37, 57–81.
- Galadini, F., Messina, P., Giaccio, B., Sposato, A., 2003. Early uplift history of the Abruzzi Apennines (central Italy): available geomorphological constraints. *Quaternary International* 101–102, 125–135.
- Galli, P., 2000. New empirical relationships between magnitude and distance for liquefaction. *Tectonophysics* 324, 169–187.
- Galli, P., Galadini, F., Moro, M., Giraudi, C., 2002. New paleoseismological data from the Gran Sassi d'Italia area (central Apennines). *Geophysical Research Letters* 29 (7): 1134. <https://doi.org/10.1029/2001GL013292>.
- Galli, P., Galadini, F., Calzoni, F., 2005. Surface faulting in Norcia (central Italy): a “paleoseismological perspective”. *Tectonophysics* 403, 117–130.
- Galli, P., Galadini, F., Pantosti, D., 2008. Twenty years of paleoseismology in Italy. *Earth-Science Reviews* 88, 89–117.
- Gardner, T.W., Ritter, J.B., Shuman, C.A., Bell, J.C., Sasowsky, K.C., Pinter, N., 1991. A periglacial stratified slope deposit in the Valley and Ridge Province of Central Pennsylvania, USA: sedimentology, stratigraphy, and geomorphic evolution. *Permafrost and Periglacial Processes* 2, 141–162.
- Geyh, M.A., 2005. *Handbuch der physikalischen und chemischen Altersbestimmung*. Wissenschaftliche Buchgesellschaft, Darmstadt 165–188 (211pp.).
- Ghisetti, F., Vezzani, L., 1991. Thrust belt development in the central Apennines: northward polarity of thrusting and out-of-sequence deformations in the Gran Sasso chain (Italy). *Tectonics* 10, 904–919.
- Ghisetti, F., Vezzani, L., 1999. Depth and models of Pliocene–Pleistocene crustal extension of the Apennines (Italy). *Terra Nova* 11, 67–72.
- Ghisetti, F., Vezzani, L., 2002. Normal faulting, extension and uplift in the outer thrust belt of the central Apennines (Italy): role of the Caramanico fault. *Basin Research* 14, 225–236.
- Ghisetti, F., Kirschner, D.L., Vezzani, L., Agosta, F., 2001. Stable isotope evidence for contrasting paleofluid circulation in thrust faults and normal faults of the central Apennines, Italy. *Journal of Geophysical Research* 106 (B5), 8811–8825.
- Giraudi, C., 1995. I detriti di versante ai margini della Piana del Fucino (Italia Centrale): Significato paleoclimatico ed impatto antropico. *Il Quaternario* 8, 203–210.
- Giraudi, C., 2005. Middle to Late Holocene glacial variations, periglacial processes and alluvial sedimentation on the higher Apennine massifs (Italy). *Quaternary Research* 64, 176–184.
- Giraudi, C., 2012. The Campo Felice Late Pleistocene glaciation (Apennines, Central Italy). *Journal of Quaternary Science* 27, 432–440.
- Giraudi, C., 2015. The upper Pleistocene deglaciation on the Apennines (Peninsular Italy). *Cuadernos de Investigación Geográfica* 41, 337–358.
- Giraudi, C., Frezzotti, M., 1995. Palaeoseismicity in the Gran Sasso massif (Abruzzo, central Italy). *Quaternary International* 25, 81–93.
- Giraudi, C., Frezzotti, M., 1997. Late Pleistocene glacial events in the Central Apennines, Italy. *Quaternary Research* 48, 280–290.
- Gori, S., Giaccio, B., Galadini, F., Falucci, E., Messina, P., Sposato, A., Dramis, F., 2011. Active normal faulting along the Mt. Morrone south-western slopes (central Apennines, Italy). *International Journal of Earth Sciences* 100, 157–171.
- Gori, S., Flacucci, E., Dramis, F., Galadini, F., Galli, P., Giaccio, B., Messina, P., Pizzi, A., Sposato, A., Cosentino, D., 2014. Deep-seated gravitational slope deformation, large-scale rock failure, and active normal faulting along Mt. Morrone (Sulmona basin, Central Italy): geomorphological and paleoseismological analyses. *Geomorphology* 208, 88–101.
- Gori, S., Falucci, E., Ladina, C., Marzorati, S., Galadini, F., 2017. Active faulting, 3-D geological architecture and Plio-Quaternary structural evolution of extensional basins in the central Apennine chain, Italy. *Solid Earth* 8, 319–337.
- Grunewald, K., Scheithauer, J., 2010. Europe's southernmost glaciers: response and adaptation to climate change. *Journal of Glaciology* 56, 129–142.
- Guises, R., Xiang, J., Latham, J.-P., Munjiza, A., 2009. Granular packing: numerical simulation and the characterization of the effect of particle shape. *Granular Matter* 11, 281–292.
- Hales, T.C., Roering, J.J., 2005. Climate-controlled variations in scree production, Southern Alps, New Zealand. *Geology* 33, 701–704.
- Hall, K., Thorn, C.E., 2014. Thermal fatigue and thermal shock in bedrock: an attempt to unravel the geomorphic processes and products. *Geomorphology* 206, 1–13.
- Heitzmann, P., 1985. Kakirite, Kataklastite, Mylonite: zur Nomenklatur der Metamorphite mit Verformungsgefügen. *Ecolgae Geologicae Helveticae* 78, 273–286.
- Hippolyte, J.-C., 2001. Palaeostress and neotectonic analysis of sheared conglomerates: Southwest Alps and Southern Apennines. *Journal of Structural Geology* 23, 421–429.
- Hughes, P.D., Woodward, J.C., Gibbard, P.L., 2006. Quaternary glacial history of the Mediterranean mountains. *Progress in Physical Geography* 30, 334–364.
- Hurst, A., Scott, A., Vigorito, M., 2011. Physical characteristics of sand injectites. *Earth-Science Reviews* 106, 215–246.
- Jolly, R.J.H., Lonergan, L., 2002. Mechanisms and controls on the formation of sand intrusions. *Journal of the Geological Society of London* 159, 805–817.
- Kastelic, V., Burrato, P., Carafa, M.M.C., Basili, R., 2017. Repeated surveys reveal nontectonic exposure of supposedly active normal faults in the central Apennines, Italy. *Journal of Geophysical Research - Earth Surface* 122. <https://doi.org/10.1002/2016JF003953>.
- Kotarba, A., Strömquist, L., 1984. Transport, sorting and deposition processes of Alpine debris slope deposits in the Polish Tatra Mountains. *Geografiska Annaler* 66A, 285–294.
- Krautblatter, M., Moser, M., 2009. A nonlinear model coupling rockfall and rainfall intensity based on a four year measurement in high Alpine rock wall (Reintal, German Alps). *Natural Hazards and Earth System Sciences* 9, 1425–1432.
- Krautblatter, M., Moser, M., Schrott, L., Wolf, J., Morche, D., 2012. Significance of rockfall magnitude and carbonate dissolution for rock slope erosion and geomorphic work on Alpine limestone cliffs (Reintal, Alps). *Geomorphology* 167–168, 21–34.
- Lavecchia, G., Brozzetti, F., Barchi, M., Menichetti, M., Keller, J.V.A., 1994. Seismotectonic zoning in east-central Italy deduced from an analysis of the Neogene to present deformations and related stress fields. *Geological Society of America Bulletin* 106, 1107–1120.
- Lavecchia, G., Adinolfi, G.M., de Nardis, R., Ferrarini, F., Cirillo, D., Brozzetti, F., De Matteis, R., Festa, G., Zollo, A., 2017. Multidisciplinary inferences on a newly recognized active east-dipping extensional system in Central Italy. *Terra Nova* 29, 77–89.
- Longiaru, S., 1987. Visual comparators for estimating the degree of sorting from plane and thin section. *Journal of Sedimentary Petrology* 57, 791–794.
- Lowe, D.R., 1976. Grain flow and grain flow deposits. *Journal of Sedimentary Petrology* 46, 188–199.
- Malinverno, A., Ryan, W.B.F., 1986. Extension in the Tyrrhenian sea and shortening in the Apennines as a result of arc migration driven by sinking of lithosphere. *Tectonics* 5, 227–245.
- Mantovani, E., Babbucci, D., Tamburelli, C., Viti, M., 2009. A review on the driving mechanisms of the Tyrrhenian-Apennines system: Implications for the present seismotectonic setting in the Central-Northern Apennines. *Tectonophysics* 476, 22–40.
- McEwen, T.J., 1981. Brittle deformation in pitted pebble conglomerates. *Journal of Structural Geology* 3, 25–37.
- Meyer, M.C., Wiesmayr, G., Brauner, M., Häusler, H., Wangda, D., 2006. Active tectonics in Eastern Lunana (NW Bhutan): implications for the seismic and glacial hazard potential of the Bhutan Himalaya. *Tectonics* 25, TC3001. <https://doi.org/10.1029/2005TC001858>.
- Micarelli, L., Benedicto, A., Wibberley, C.A.J., 2006. Structural evolution and permeability of normal fault zones in highly porous carbonate rocks. *Journal of Structural Geology* 28, 1214–1227.
- Mohindra, R., Bagati, T.N., 1996. Seismically induced soft-sediment deformation structures (seismites) around Sumdo in the lower Spiti valley (Tethys Himalaya). *Sedimentary Geology* 101, 69–83.
- Molano, J.L., McKay, C.P., 2010. Processes controlling rapid temperature variations on rock surfaces. *Earth Surface Processes and Landforms* 35, 501–507.
- Montone, P., Mariucci, M.T., Pondrelli, S., Amato, A., 2004. An improved stress map for Italy and surrounding regions. *Journal of Geophysical Research* 109, B10410. <https://doi.org/10.1029/2003JB002703>.
- Moore, J.R., Sanders, J.W., Dietrich, W.E., Glaser, S.D., 2009. Influence of rock mass strength on the erosion rate of alpine cliffs. *Earth Surface Processes and Landforms* 34, 1339–1352.
- Obermeier, S.F., 1996. Use of liquefaction-induced features for paleoseismic analysis – an overview of how seismic liquefaction features can be distinguished from other features and how their regional distribution and properties of source sediment can be used to infer the location and strength of Holocene paleo-earthquakes. *Engineering Geology* 44, 1–76.

- Olyphant, G.A., 1983. Analysis of the factors controlling cliff burial by talus within Blanca Massif, southern Colorado, U.S.A. *Arctic and Alpine Research* 15, 65–75.
- Ortner, H., 1996. Deformation und Diagenese im Unterinntaler Tertär (zwischen Rattenberg und Durchholzen) und seinem Rahmen. (PhD thesis). University of Innsbruck (234 pp.).
- Ortner, H., Reiter, F., Acs, P., 2002. Easy handling of tectonic data: the programs TectonicVB for Mac and TectonicsFP for Windows(TM). *Computers & Geosciences* 28, 1193–1200.
- Ortner, H., Pomella, H., Sanders, D., 2014. Formation of cataclases in shallow-subsurface settings – meteoric diagenetic processes control fault rock formation at seismogenic faults in the Abruzzi Apennines, Italy. *Geophysical Research Abstracts* 16, EGU2014-6971-1.
- Ortner, H., Sanders, D., Pomella, H., 2018. Normal fault morphology and ageing of cataclases at Campo Imperatore, Abruzzi Apennines, Italy. *Geophysical Research Abstracts* 20, EGU2018-8969.
- Ostermann, M., Sanders, D., 2016. The Brenner pass rock avalanche cluster suggests a close relation between long-term slope deformation (DSGSDs and translational rockslides) and catastrophic failure. *Geomorphology* 289, 44–59.
- Ostermann, M., Sanders, D., Prager, C., Kramers, J., 2007. Aragonite and calcite cementation in 'boulder-controlled' meteoric environments on the Fern Pass rockslide (Austria): implications for radiometric age-dating of catastrophic mass movements. *Facies* 53, 189–208.
- Ostermann, M., Ivy-Ochs, S., Sanders, D., Prager, C., 2016. Multi-method (^{14}C , ^{36}Cl , ^{234}U / ^{230}Th) age bracketing of the Tschirgant rock avalanche (Eastern Alps): implications for absolute dating of catastrophic mass-wasting. *Earth Surface Processes and Landforms* 42, 1110–1118.
- Ouellet, M.-A., Germain, D., 2014. Hyperconcentrated flows on a forested alluvial fan of eastern Canada: geomorphic characteristics, return period, and triggering scenarios. *Earth Surface Processes and Landforms* 39, 1876–1887.
- Owen, G., 1995. Soft-sediment deformation in upper Proterozoic Torridonian sandstones (Applecross Formation) at Torridon, northwest Scotland. *Journal of Sedimentary Research* A65, 495–504.
- Owen, G., 1996. Experimental soft-sediment deformation: structures formed by the liquefaction of unconsolidated sands and some ancient examples. *Sedimentology* 43, 279–293.
- Ozouf, J.-C., Texier, J.-P., Bertran, P., Coutard, J.-P., 1995. Quelques coupes caractéristiques dans les dépôts de versant d'Aquitaine septentrionale: Faciès et interprétation dynamique. *Permafrost and Periglacial Processes* 6, 89–101.
- Papanikolaou, I.D., Roberts, G.P., Michetti, A.M., 2005. Fault scarps and deformation rates in Lazio-Abruzzo, Central Italy: comparison between geological fault-slip rate and GPS data. *Tectonophysics* 408, 147–176.
- Patacca, E., Sartori, R., Scandone, P., 1990. Tyrrhenian Basin and Apenninic arcs: kinematic relations since late Tortonian times. *Memorie della Società Geologica Italiana* 45, 425–451.
- Pizzi, A., 2003. Quaternary uplift rates in the outer zone of the central Apennines fold-and-thrust belt, Italy. *Quaternary International* 101-102, 229–237.
- Pizzi, A., Falucci, E., Gori, S., Galadini, F., Messina, P., Di Vincenzo, M., Esetime, P., Giaccio, B., Pomposo, G., Sposato, A., 2010. Active faulting in the Maiella massif (central Apennines, Italy). *GeoActa Special Publication* 3, 57–73.
- Reid, E., Thomas, M.F., 2006. A chronostratigraphy of mid and late-Holocene slope evolution: Creagan a' Chaorainn, Northern Highlands, Scotland. *The Holocene* 16, 429–444.
- Roberts, G.P., Michetti, A.M., 2004. Spatial and temporal variations in growth rates along active normal fault systems: an example from the Lazio-Abruzzo Apennines, central Italy. *Journal of Structural Geology* 26, 339–376.
- Ross, J.A., Peakall, J., Keevil, G.M., 2011. An integrated model of extrusive sand injectites in cohesionless sediments. *Sedimentology* 58, 1693–1715.
- Sanders, D., 2010. Sedimentary facies and progradational style of a Pleistocene talus-slope succession, Northern Calcareous Alps, Austria. *Sedimentary Geology* 228, 271–283.
- Sanders, D., 2012. Talus accumulation in detachment scars of late Holocene rock avalanches, Eastern Alps (Austria): rates and implications. *GeoAlp* 9, 82–99.
- Sanders, D., 2013. Features related to snow avalanches and snow glides, Nordkette range (Northern Calcareous Alps). *GeoAlp* 10, 71–92.
- Sanders, D., 2016. Neotectonic deformation in Quaternary deposits, Northern Calcareous Alps (abstr.). *GeoTirolo 2016—Annual Meeting DGGV, Abstract Volume*, p. 294.
- Sanders, D., Ostermann, M., 2011. Post-last glacial alluvial fan and talus slope associations (Northern Calcareous Alps, Austria): a proxy for Late Pleistocene to Holocene climate change. *Geomorphology* 131, 85–97.
- Sanders, D., Ostermann, M., Kramers, J., 2009. Quaternary carbonate-rocky talus slope successions (Eastern Alps, Austria): sedimentary facies and facies architecture. *Facies* 55, 345–373.
- Sanders, D., Ostermann, M., Brandner, R., Prager, C., 2010a. Meteoric lithification of cataclastic rockslide deposits: diagenesis and significance. *Sedimentary Geology* 223, 150–161.
- Sanders, D., Ostermann, M., Kramers, J., 2010b. Meteoric diagenesis of Quaternary carbonate-rocky talus slope successions (Northern Calcareous Alps, Austria). *Facies* 56, 27–46.
- Sanders, D., Widera, L., Ostermann, M., 2014. Two-layer scree/snow-avalanche triggered by rockfall (Eastern Alps): significance for sedimentology of scree slopes. *Sedimentology* 61, 996–1030.
- Sanders, D., Ortner, H., Pomella, H., 2018. Meteoric diagenesis of ultracataclases records late-stage fault movement, central Apennines, Italy. *Geophysical Research Abstracts* 20, EGU2018-11823-1.
- Sass, O., 2005. Spatial patterns of rockfall intensity in the northern Alps. *Zeitschrift für Geomorphologie Supplementband* 138, 51–65.
- Sibson, R.H., 1977. Fault rocks and fault mechanisms. *Journal of the Geological Society of London* 133, 191–213.
- Simon, J.L., 2007. Analysis of solution lineations in pebbles: kinematical vs. dynamical approaches. *Tectonophysics* 445, 337–352.
- Sinnott, M.D., Cleary, P.W., 2009. Vibration-induced arching in a deep granular bed. *Granular Matter* 11, 345–364.
- Sohn, Y.K., Rhee, C.W., Kim, B.C., 1999. Debris flow and hyperconcentrated flood-flow deposits in an alluvial fan, northwestern part of the Cretaceous Yongdong Basin, central Korea. *The Journal of Geology* 107, 111–132.
- Spötl, C., Vennemann, T.W., 2003. Continuous-flow isotope ratio mass spectrometric analysis of carbonate minerals. *Rapid Communications in Mass Spectrometry* 17, 1004–1006.
- Summerfield, M.A., 1991. *Global Geomorphology*. Longman Scientific & Technical, Essex (537 pp.).
- Tondi, E., Cello, G., 2003. Spatiotemporal evolution of the Central Apennines fault system (Italy). *Journal of Geodynamics* 36, 113–128.
- Tuitz, C., Exner, U., Grasemann, B., Preh, A., 2010. Who cracked the pebbles in the gravel pit—lithostatic pressure or a bunch of faults? *Geophysical Research Abstracts* 12, EGU2010-9762-2.
- Tuitz, C., Exner, U., Frehner, M., Grasemann, B., 2012. The impact of ellipsoidal particle shape on pebble breakage in gravel. *International Journal of Rock Mechanics and Mining Sciences* 54, 70–79.
- Valoroso, L., Chiaraluce, L., Colletini, C., 2014. Earthquakes and fault zone structure. *Geology* 42, 343–346.
- Van Steijn, H., 1988. Debris flows involved in the development of Pleistocene stratified slope deposits. *Zeitschrift für Geomorphologie, Neue Folge, Supplementband* 71, 45–58.
- Van Steijn, H., 2011. Stratified slope deposits: Periglacial and other processes involved. In: Martini, I.P., French, H.M., Pérez Alberti, A. (Eds.), *Ice-marginal and Periglacial Processes and Sediments*. Geological Society of London, Special Publications 354, pp. 213–226.
- Van Steijn, H., Bertran, P., Francou, B., Hétu, B., Texier, J.-P., 1995. Models for the genetic and environmental interpretation of stratified slope deposits: review. *Permafrost and Periglacial Processes* 6, 125–146.
- Ventra, D., Chong Diaz, G., De Boer, P.L., 2013. Colluvial sedimentation in a hyperarid setting (Atacama Desert, northern Chile). *Geomorphological controls and stratigraphic facies variability*. *Sedimentology* 60, 1257–1290.
- Viti, M., Mantovani, E., Babbucci, D., Tamburelli, C., 2011. Plate kinematics and geodynamics in the Central Mediterranean. *Journal of Geodynamics* 51, 190–204.
- Watanabe, T., Dali, L., Shiraiwa, T., 1998. Slope denudation and the supply of debris to cones in Langtang Himal, Central Nepal Himalaya. *Geomorphology* 26, 185–197.
- Woodcock, N.H., Mort, K., 2008. Classification of fault breccias and related fault rocks. *Geological Magazine* 145, 435–440.
- Young, A., 1961. Characteristic and limiting slope angles. *Zeitschrift für Geomorphologie* 5, 126–131.